FISSION BARRIER
OF PRE - ACTINDE NUCLEI
USING COVARIANT DENSITY FUNCTIONAL THEORY

حاجز الطاقة للانشطار النووي في انوية عناصر ما قبل الاكتينيدات باستخدام النظرية الوظيفية للكثافة المتغيرة

A thesis submitted in partial fulfillment
of the requirements for the Masters degree
in Physics

Doaa Ibrahim DarTaha

Supervised by :
Dr. Hazem Abusara

BIRZEIT UNIVERSITY
Birzeit, Palestine

2019

FISSION BARRIER
OF PRE - ACTINDE NUCLEI
USING COVARIANT DENSITY FUNCTIONAL THEORY

حاجز الطاقة للانشطار النووي في انوية عناصر ما قبل الاكتينيدات باستخدام النظرية الوظيفية للكثافة المتغيرة

A thesis submitted in partial fulfillment
of the requirements for the Masters degree
in Physics

Doaa Ibrahim DarTaha

Supervised by :
Dr. Hazem Abusara

BIRZEIT UNIVERSITY
Birzeit, Palestine

2019

FISSION BARRIER
OF PRE - ACTINDE NUCLEI
USING COVARIANT DENSITY FUNCTIONAL THEORY

A thesis submitted in partial fulfillment
of the requirements for the Masters degree
in Physics

By:
Doaa Ibrahim DarTaha

Thesis committee :
Dr. Hazem Abusara (Principle advisor)
Dr. Wafaa Khater (Member)
Dr. Esmael Badran (Member)

This Thesis was submitted in partial fulfillment of the requirements for the Master Degree in Physics from the Factually Graduated Studies at Birzeit, Palestine

2019

Declaration

I, Doaa DarTaha, declare that this thesis titled, 'FISSION BARRIER OF PRE - ACTINDE NUCLEI USING COVARIANT DENSITY FUNCTIONAL THEORY' and the work presented in it are my own

Dr. Hazem Abusara (Supervisor):

Dr. Wafaa Khater (Committee Member) :

Dr. Esmael Badran (Committee Member) :

Dedication

To my father, who has been the source of love and encouragement to me throughout my life, thank you for always being with me. To my mother and mother-in-law, whose love and prayers are with me. To my loving husband, thanks for being so supportive. To my whole family, my brothers and sisters for their continues support, you all count so much, thank you all.

Acknowledgements

First and foremost, I am indebted to my thesis supervisor Dr. Hazem Abusara for his support, guidance and patience through this work. I can never forget all the help you have provided me. Thank you so much!

I am grateful to all of my Doctors, for the experience they have helped me gain by studying and working at the Department of Physics. I would especially like to thank members of my committee, Dr. Wafaa Khater and Dr. Esmael Badran, for reviewing my thesis. Thank you for your helpful feedback.

Abstract

Systematic calculations of fission barriers, are performed for even-even pre-actinide nuclei, in the range of proton numbers $80 \leq Z \leq 86$ and neutron numbers $94 \leq N \leq 148$, within covariant density functional theory. Our calculations are carried out in the relativistic-Hartree-Bogoliubov framework, based on density-dependent zero and finite range interactions, imposing axially symmetric deformations.

The saddle-point and ground-state energies, are determined from potential energy curves, defined by the elongation deformation parameter β_2. The barriers heights B_f are calculated, as the difference between the highest saddle-point and the ground-state energy. The observed fission barriers heights and positions, are independent of the choice of parametrization, for all of the nuclei in question. Comparisons with experimental data and different theoretical calculations are also shown.

The tabulated barriers in this investigated region are from 3.8 to 20.8 MeV. Only for Hg ($98 \leq N \leq 102$) and Pb ($N = 178, 180$), more than one saddle point has been observed, while the rest Hg, Pb, Po and Rn isotopic chain show a single barrier.

in the whole region of considered nuclei, the same data trends are observed. For a given value of Z, we observed a saddle point emergence to a lower deformation, as N increases, with some isotopic variation at the end of each isotopic chain. The barrier height increases with N, the highest barrier is obtained at $N = 126$, then with increasing N the barrier fall to a minimum at around $N = 140$. While the height of the barrier remains remarkably constant as Z increase, for a given value of N.

The comparison with experiment covers only few number of isotopes, in this restricted region. The largest discrepancy with the experimental data, is obtained for Hg isotopes, the agreement is better for Pb, Po and Rn isotopes.

ملخص

نجري في هذه الدراسة حسابات ممنهجة لحاجز الطاقة للانشطار النووي لسلسلة من نظائر الزئبق والرصاص والبولونيوم والرادون ضمن النظرية الوظيفية للكثافة المتغيرة، باستخدام تفاعلات النيوكلونات الصفرية والمحدودة، للانوية التي تحقق تماثل محوري خلال الانشطار.

نقوم بحساب طاقة حاجز الانشطار من خلال الفرق بين قيمة اعلى وادنى نقاط للحاجز على منحنى طاقة الوضع. وقد تبين ان ارتفاع و موقع حاجز الانشطار لا يعتمد على النموذج المستخدم في الحسابات سواء كان نموذج التفاعل غير الخطي أو نموذج التفاعل الكثافي الصفري والمحدود. كما ونقارن نتائج حساباتنا بالقيم العملية و النظرية المتوفرة.

تراوحت قيمة الطاقة لحواجز الانشطار المحسوبة للأنوية المذكورة من (٣،٨) إلى (٢٢،٨) مليون إلكترون فولت، نلاحظ وجود حاجز انشطار ذو قمتين في كل من نظائر الزئبق عند (ن = ٩٨، ١٠٠، ١٠٢) ونظيري الرصاص عند (ن = ١٧٨، ١٨٠) في حين ظهور حاجز انشطار احادي القمة لباقي النظائر .

تبين لنا في العلاقة بين عامل الاستطالة و عدد النيوترونات الاتي: كلما زاد عدد النيوترونات يكون عامل الاستطالة اقل، عدا نهايات سلاسل النظائر. يزداد ارتفاع حاجز الانشطار مع عدد النيوترونات. يكون أعلى حاجز طاقة عند عدد النيوترونات (ن = ١٢٦)، ويتناقص للقيم (ن > ١٢٦) ويبلغ قيمته الدنيا عند (ن = ١٤٤) ويبقى ارتفاع حاجز الطاقة ثابتا تقريبا مع زيادة العدد الذري لعدد نيوترونات معين.

لا تشمل مقارنة نتائجنا مع القيم العملية سوى عدد قليل من النظائر. تباينت نتائج النموذج مع القيم العملية لنظائر الزئبق، في حين ان النتائج تطابقت بشكل افضل مع تلك العملية في حالة الرصاص والبولونيوم والرادون .

Contents

List of Figures

List of Tables

Chapter 1
Introduction

Early calculations of fission barriers were based on the macroscopic-microscopic (MM) framework. In this framework, the total potential energy of a nucleus is calculated as the sum of a macroscopic term and a microscopic term. The MM approach has been used with remarkable success, to calculate fission barriers of actinide nuclei [1–5]. Most of these calculations, that emphasize on the fission barrier of heavy elements, have been performed only for a limited number of nuclei. Also, nor mass asymmetric neither axially asymmetric shape distortions were included. the calculations of Refs.[1] and [5] were in good agreement with fission-barrier data in the actinide region.

In the study of Ref.[4], 1125 neutron-rich nuclei in the heavy-element region, with $76 \leq Z \leq 100$ and $140 \leq N \leq 184$, were of interest in connection with the MM model. Odd nuclei were included, and the effects of mass-asymmetric and axially asymmetric shape distortions were also taken into account.

Soon afterwards, in 1984, H.Stroher et al. [6] enabled to deduce fission barriers for a number of pre-actinide nuclei form electrofission experiments. The work was

intended to experimentally test the theoretical predictions, based on MM models on the fission of ^{182,184,186}W, ^{nat}Pt and ^{209} Bi nuclei. This was possible by measuring absolute electrofission cross sections σ_{ef} in the energy range between 25 and 55 MeV.

The subsequent studies [7–14] then extended to account for fission barrier heights in other regions of nuclear masses, such as pre-actinidde region. In Ref.[7], Moller et al. presented calculations of nuclear ground-state masses and deformations, permeated by a calculation of heights of the outer peak in the fission barrier of 28 nuclei, including pre-actinide nuclei, based on an improved MM model. This model successfully account for fission barrier heights of all of these nuclei.

In nuclear fission, the nucleus deform to separate into two fragments. Calculations of fission barriers need the determination of the total nuclear potential energy, with different nuclear shapes. A large deformation space, with five shape degrees of freedom corresponding to elongation, neck radius, left-fragment shape, right-fragment shape, and the asymmetry of the mass division, have been used to calculate fission barriers, in different nuclear mass regions [8–11], instead to one with 3 degrees of freedom, previously used to determine the locations and heights of the fission saddle points [7]. Moreover the calculation of Ref.[11], was performed from ^{70}Se to ^{252}Cf, taking into account a higher-dimensional deformation space with over 10000 times as many deformation points as in previous calculations. Such a calculation found that the saddles for a given nucleus, are lower than those found in early (1995, 2000) studies [8, 10], with the same model parameters.

There have already been a number of models for the nuclear potential energy. A self-consistent mean-field (SMF) model using effective forces, for example, a Hartree-Fock (HF) or Hartree-Fock-Bogolyubov (HFB) model with Skyrme or Gogny effective interactions [15, 16], have been presented in the past decades. However, it was difficult to locate a reliable saddle-point configuration in SMF models. In an attempt to make a reliable fission barriers calculation, Mamdouh et al. developed The first systematic microscopic calculation [17], which is based on the ETFSI (extended Thomas-Fermi plus Strutinsky integral), a high-speed approximation to the Skyrme-HF method, with pairing treated in the BCS approximation. This calculation involved large number of barriers, for nuclei in the range of proton numbers $66 \leq Z \leq 100$ and neutron numbers $94 \leq N \leq 157$, assuming axially symmetrical deformations. The ETFSI method then has been extended to include triaxiality. Such calculation was carried out for all of the nearly 2000 nuclei in the range of proton numbers $84 \leq Z \leq 120$, including all the neutron-rich nuclei up to $A = 318$ [18].

There exist, of course, many self-consistent mean-field calculations for fission barriers: Three effective ones are, [19, 20] and [21]. The latter giving a large-scale fission barrier calculations within the Skyrme-Hartree-Fock framework, in pre-actinide and actinide regions. A large set of Skyrme interactions was used, to see how well a force affect the barrier heights. In this investigation, axial symmetry was imposed with quadrupole, octupole, and hexadecapole degrees of freedom, but reflection asymmetry was allowed.

Another important calculation, is the one preformed by Moller et al. in 2009 [12]. The barriers are calculated in the macroscopic-microscopic finite-range liquid-drop model(FRLDM), for 1585 nuclei throughout the periodic table, including the pre-actinide nuclei. Within the macroscopic-microscopic approach, Kowal et al. [22] calculated fission barrier heights B_f for even-even heavy and superheavy nuclei, to determine their survival probability against spontaneous fission. Higher nonaxial and reflection-asymmetric degrees of freedom were considered, in contrast to SHF models.

However, developments in the area of nuclear fission, show that these earlier studies can now be improved due to three reasons: The advances in computation power at hand, the technology we have to produce more experimental data, and the vast models that scientists develop. For example, Moller et al. [23] enabled to extend their calculation and tabulate barriers for 5239 nuclides, for all nuclei between the proton and neutron drip lines in the mass range 171-330, exactly as described in Ref.[12]. The saddle-point heights were determined from potential-energy surfaces, based on millions of shapes. This was a problem when they started this type of calculation in 1999 [9]; now it not.

As we have already discussed, the investigation of fission barriers, in the pre-actinide region were performed in the following frameworks: microscopic+macroscopic (MM) methods [7, 9, 11, 12, 23], the extended Thomas-Fermi plus Strutinsky integral (ETFSI) method [17, 18], and the Skyrme-Hartree-Fock framework [21].

Recently, the current works in nuclear fission process emphasis on heavy and superheavy nuclei (Z $\geq$ 100) within the frameworks of the microscopic + macroscopic method [23, 24], and covariant density functional theory (CDFT) [25–28]. The later approach was employed to replace the non relativistic energy density functionals (EDF) methods [29, 30], previously used, built on Lorentz covariance and the Dirac equation, leading to realistic description for fission barriers for such nuclei. For example, within covariant density functional theory, H Abusara et al. [25] presented the first systematic investigation of triaxial fission barriers, in the actinide region. It was found that the height of the inner fission barrier is reduced due to triaxial deformations by $1-4$ MeV. These results were in reasonable agreement with data comparable with MM calculations.

Two years later, H Abusara et al. [26] then extrapolated to even-even superheavy nuclei with $z = 112 - 120$. This was also the first systematic investigations of fission barriers in superheavy region within covariant density functional theory, taking into account the triaxial deformation. Three different classes of models with parameterizations NL3*, DD-ME2 and DD-PC1 were used in the calculations.

In the present work, we apply covariant density functional theory (CDFT) within relativistic-Hartree-Bogoliubov (RHB) framework, based on NL3*, DD-ME2, and DD-PC1 forces, to obtain potential energy curves (PEC) and barrier heights B_f, in the pre-actinide region for Hg, Pb, Po and Rn isotopes. The main purpose is to perform new calculations of fission barriers in this investigated region. The new results are compared with the available experimental data and other theoretical approaches results. An additional goal is to see how the choice of the specific

CDFT model influencing the barrier heights.

This thesis is outlined as follows: CHAPTER 2 deals with CDFT models in the RHB framework, and the details of the numerical calculations. In CHAPTER 3, we deliver PEC, barrier heights, and a comparison of calculated data to the experimentally and theoretically known cases of Hg, Pb, Po, and Rn isotopes, respectively. Conclusions are given in CHAPTER 4.

Chapter 2

Formalism

2.1 Covariant Density Functional Theory (CDFT)

The Covariant Density functional Theory is widely used in the field of nuclear structure. The CDFT [31, 32] is one of the most successful theories, for a microscopic description of the nuclear structure properties, such as binding energy, radii, and deformation parameters. Based on ideas of effective field theory, nonlinear interactions between the fields are introduced to parameterize the density dependence of the energy functional.

Different models have been developed, that reproduce the same observed nuclear properties. The three models we treat here are: the nonlinear meson nucleon coupling model (NL), the density-dependent meson nucleon coupling model (DD-ME), and a density-dependent point coupling model (DD-PC). The interaction in the first two models has a finite range, while the third model uses zero-range interaction [33–36]. The mesons are absent in the density-dependent point coupling

model. The density dependence is explicit in the last two models, while it shows up via the non- linearity in the σ-meson in the nonlinear meson-nucleon coupling model.

2.2 Lagrange density and field equations

In this formulation, we starts with Lagrangian density, the nucleons are treated as Dirac spinor ψ, interacting via the exchange of point-like particles, called mesons (scalar σ, vector ω, and vectorρ) and photon fields.

The total Lagrangian density for nucleons and mesons $\mathcal{L}$ is :

$$\mathcal{L} = \mathcal{L}^{free}_{Nucleon} + \mathcal{L}^{free}_{Meson} + \mathcal{L}^{int}_{NM} \tag{2.1}$$

$\mathcal{L}^{free}_{Nucleon}$ denotes the Lagrangian of the free nucleon

$$\mathcal{L}^{free}_{Nucleon} = \overline{\psi}_i(i\gamma^\mu\partial_\mu - M)\psi_i \tag{2.2}$$

$\mathcal{L}^{free}_{Meson}$ is the Lagrangian for the free meson fields and electromagnetic field

$$\begin{aligned}\mathcal{L}^{free}_{Meson} = & -\frac{1}{2}\partial^\mu\sigma\partial_\mu\sigma - U(\sigma) - \frac{1}{4}\Omega^{\mu\nu}\Omega_{\mu\nu} + \frac{1}{2}m^2_\omega\omega^\mu\omega_\mu \\ & -\frac{1}{4}R^{\mu\nu}R_{\mu\nu} + \frac{1}{2}m^2_\rho\rho^\mu\rho_\mu - \frac{1}{4}F^{\mu\nu}F_{\mu\nu}\end{aligned} \tag{2.3}$$

$\mathcal{L}_{NM}^{int}$ contains the nucleon-meson interaction terms

$$\mathcal{L}_{NM}^{int} = -g_\sigma \overline{\psi}_i \psi_i \sigma - g_\omega \overline{\psi}_i \gamma^\mu \psi_i \omega_\mu - g_\rho \overline{\psi} \gamma^\mu \tau \psi_i \rho_\mu - e \overline{\psi}_i \gamma^\mu \frac{1+\tau_3}{2} \psi_i A_\mu \quad (2.4)$$

The above equations contain the nucleon mass M, the meson masses, m_σ , m_ω, and m_ρ, and the coupling constants g_σ, g_ω, and g_ρ. e is the charge of the protons and it vanishes for neutrons.

$\tau(\tau_3)$ denotes isotopic spin (third component of τ) for the nucleon spinor, τ_3 is -1 for a neutron and $+1$ for proton. The field-strength tensors $\Omega^{\mu\nu}$, $R^{\mu\nu}$ corresponding to the ω and ρ mesons, and the tensor $F^{\mu\nu}$ corresponding to the electromagnetic field, appearing in the Lagrangian are given by

$$\Omega^{\mu\nu} = \partial^\mu \omega^\nu - \partial^\nu \omega^\mu \quad (2.5)$$

$$R^{\mu\nu} = \partial^\mu \rho^\nu - \partial^\nu \rho^\mu \quad (2.6)$$

$$F^{\mu\nu} = \partial^\mu A^\nu - \partial^\nu A^\mu \quad (2.7)$$

The field equations result from the Euler-Lagrange equations

$$\partial_\mu \left(\frac{\partial \mathcal{L}}{\partial(\partial_\mu \Phi)}\right) - \frac{\partial \mathcal{L}}{\partial \Phi} = 0 \quad , \quad (2.8)$$

where Φ can be substituted by $\psi, \overline{\psi}, \sigma, \omega_\mu$.

We obtain the Dirac equation in the medium:

$$[\gamma_\mu(i\partial^\mu - g_\omega\omega^\mu) - (M - g_\sigma\sigma)]\psi \quad = \quad 0 \tag{2.9}$$

And the meson-field equations :

1. The Klein-Gordon equation with a source-term :

$$(\partial_\mu\partial^\mu + m_\sigma^2)\sigma \quad = \quad g_\sigma\overline{\psi}\psi \tag{2.10}$$

2. The Proca equation with a source-term $\equiv$ massive Maxwell equation :

$$\partial^\nu\Omega_{\mu\nu} + m_\omega^2\omega_\mu \quad = \quad g_\omega\overline{\psi}\gamma_\mu\psi \tag{2.11}$$

2.2.1 The meson-exchange model

In the meson-exchange model, we treat protons and neutrons as point like particles, interact by the exchange of σ, ω and ρ mesons, and the photon [37, 38]. These mesons are characterized by three quantum numbers; spin (J), parity (P) and isospin (T) as the following :

1. scalar σ-meson (iso-scalar), with quantum numbers (J = 0, T = 0 , P =1), and it cause a strong attractive central force.

2. vector ω-meson (iso-scalar), with quantum numbers (J=1, T=0, P=-1), and it cause a strong repulsive central force.

3. vector ρ-meson (iso-vector), with quantum numbers (J=1, T=1, P=-1), and it couple to the iso-vector current.

The general form of the relativistic Lagrangian density describes the nuclear system :

$$\begin{aligned} \mathcal{L} = & \ \overline{\psi}[\gamma^{\mu}(i\partial_{\mu} - g_{\omega}\omega_{\mu} - g_{\rho}\vec{\rho}_{\mu}\cdot\vec{\tau} - eA_{\mu}) - M - g_{\sigma}\sigma]\psi \\ + & \ \frac{1}{2}\partial^{\mu}\sigma\partial_{\mu}\sigma - \frac{1}{2}m_{\sigma}^{2}\sigma^{2} - \frac{1}{4}\Omega_{\mu\nu}\Omega^{\mu\nu} + \frac{1}{2}m_{\omega}^{2}\omega^{\mu}\omega_{\mu} \\ - & \ \frac{1}{4}\vec{R}_{\mu\nu}\cdot\vec{R}^{\mu\nu} + \frac{1}{2}m_{\rho}^{2}\vec{\rho}^{\mu}\cdot\vec{\rho}_{\mu} - \frac{1}{4}F_{\mu\nu}F^{\mu\nu} \end{aligned} \tag{2.12}$$

The Lagrangian (2.12) contains as parameters, the meson masses m_{σ}, m_{ω}, and m_{ρ}, the coupling constants g_{σ}, g_{ω}, and g_{ρ}, and the charge of the protons e.

In this model, to treat the density dependence, Boguta and Bodmer [39] introduced a density dependence via a non-linear meson coupling, replacing the mass term $\frac{1}{2}m_{\sigma}\sigma^{2}$ in Eq.(2.12) by a quartic potential given by :

$$U(\sigma) = \frac{1}{2}m_{\sigma}\sigma^{2} + \frac{1}{3}g_{2}\sigma^{3} + \frac{1}{4}g_{3}\sigma^{4} \tag{2.13}$$

A self-interacting ω-meson, replacing the mass term by a quadratic a potential of the form :

$$U(\omega_\mu) = \frac{1}{2}m_\omega^2\omega^2 + \frac{1}{4}c_3\omega^2 \tag{2.14}$$

And a self-interacting ρ mesons, replacing the mass term by the same quadratic a potential :

$$U(\rho_\mu) = \frac{1}{2}m_\rho^2\rho^2 + \frac{1}{4}c_3\rho^2 \tag{2.15}$$

The parameters g_2, g_3 and c_3, in the equations above, are adjusted to the surface properties of finite nuclei. The nonlinear meson-nucleon coupling is represented by the parameter set NL3* [40] given in Table 2.1.

The density dependent meson-nucleon coupling model has an explicit density dependence for the meson-nucleon vertices. The coupling constant dependence is defined as :

$$g_i(\rho) = g_i(\rho_{sat})f_i(x) \quad ,(i = \sigma, \omega, \rho) \tag{2.16}$$

i can be any of the three mesons σ, ω, and ρ, where the density dependence for σ and ω is given by :

$$f_i(x) = a_i\frac{1 + b_i(x + d_i)^2}{1 + c_i(x + d_i)^2} \tag{2.17}$$

And for the ρ meson is given by :

$$f_\rho(x) = e^{-a_\rho(x-1)} \tag{2.18}$$

x is defined as the ratio between the baryonic density ρ at a specific location, and the baryonic density at saturation ρ_{sat}, in symmetric nuclear matter.

The eight parameters are not independent, but constrained as follows: $f_i(1) = 1$, $f''_\sigma(1) = f''_\omega(1)$, and $f''_i(0) = 0$. These constrains reduce the number of independent parameters, for density dependence to three. In our study this model is represented by the parameter set DD-ME2 [41] given in Table 2.1.

TABLE 2.1: NL3* and DD-ME2 parameterizations in RMF Lagrangian. Note that $g_\sigma = g_\sigma(\rho_{sat})$, $g_\omega = g_\omega(\rho_{sat})$ and $g_\rho = g_\rho(\rho_{sat})$ in the case of the DD-ME2 parametrization.

Parameter	NL3*	DD-ME2
m	939	939
m_σ	502.5742	550.1238
g_σ	10.0944	10.5396
g_2	-10.8093	-
g_3	-30.1486	-
a_σ	0.00000	1.3881
b_σ	0.00000	1.0943
c_σ	0.00000	1.7057
d_σ	0.00000	0.4421
m_ω	782.600	783.000
g_ω	12.8065	13.0189
a_ω	0.00000	1.3881
b_ω	0.00000	0.9240
c_ω	0.00000	1.4620
d_ω	0.00000	0.4775
m_ρ	763.000	763.000
g_ρ	4.5748	3.6836
a_ρ	0.00000	0.5647

2.3 The point-coupling model

In the point coupling models, the nucleons only interact with each other through effective interaction point, without exchanging mesons.

The Lagrangian for the density point coupling model [42, 43] is given by :

$$\begin{aligned}\mathcal{L} &= \bar{\psi}\left(i\gamma_\mu\partial^\mu - M\right)\psi - \frac{1}{2}\alpha_S(\hat{\rho})\left(\bar{\psi}\psi\right)\left(\bar{\psi}\psi\right) - \frac{1}{2}\alpha_V(\hat{\rho})\left(\bar{\psi}\gamma^\mu\psi\right)\left(\bar{\psi}\gamma_\mu\psi\right) \\ &- \frac{1}{2}\alpha_{TV}(\hat{\rho})\left(\bar{\psi}\vec{\tau}\gamma^\mu\psi\right)\left(\bar{\psi}\vec{\tau}\gamma_\mu\psi\right) - \frac{1}{2}\delta_S\left(\partial_v\bar{\psi}\psi\right)\left(\partial^v\bar{\psi}\psi\right) \\ &- e\bar{\psi}\gamma_\mu A^\mu\frac{(1+\tau_3)}{2}\psi \end{aligned} \tag{2.19}$$

Eq.(2.19) contains the free-nucleon Lagrangian, the point coupling interaction terms, and the coupling of the proton to the electromagnetic field. This model contains isosclar-scalar, isoscalar-vector, and isovector-vector interactions.

The coupling constant dependence is defined as :

$$\alpha_i = a_i + (b_i + c_i x)e^{-d_i x} \quad ,(i = S, V, TV), \tag{2.20}$$

where $x = \rho/\rho_{sat}$, ρ_{sat}denotes the nucleon density at saturation in symmetric nuclear matter. In our study this model is represented by the DD-PC1 parameter set given in Table 2.2.

TABLE 2.2: DD-PC1 parameterization in RMF Lagrangian.

Parameter	DD-PC1
m	939
a_σ	-10.04616
b_σ	-9.15042
c_σ	-6.42729
d_σ	1.37235
a_ω	5.91946
b_ω	8.86370
d_ω	0.65835
b_ρ	1.83595
d_ρ	0.64025

2.4 Hamiltonian density and the solution of the CDFT equations

The Hamiltonian density, corresponding to the Lagrangian density in Eq.(2.12) is:

$$\mathcal{H}(r) = \sum_m \pi_m \dot{\phi_m} - \mathcal{L}(r) \tag{2.21}$$

Where $\phi_m = (\psi,\, \sigma,\, \omega_\mu,\, \vec{\rho_\mu},\, A_\mu)$, and π_m is the conjugate momentum for the field

$$\pi_m = \frac{\partial \mathcal{L}}{\partial \dot{\phi_m}} \tag{2.22}$$

To obtain the Hamiltonian, we integrate this density over space

$$H = \int \partial^3 r \mathcal{H}(r) \tag{2.23}$$

The total Hamiltonian density for nucleons and mesons $\mathcal{H}$ is :

$$\mathcal{H} = \mathcal{H}_{Nucleon} + \mathcal{H}_{Meson} + \mathcal{H}_{int} \tag{2.24}$$

These are given by

$$\mathcal{H}_{Nucleon} = \bar{\psi}(\alpha \cdot \pi + \beta m)\psi \tag{2.25}$$

$$\begin{aligned} \mathcal{H}_{Meson} &= \mathcal{H}_{\sigma} + \mathcal{H}_{\omega} + \mathcal{H}_{\rho} \\ &= [-\frac{1}{2}\sigma\Delta\sigma + U_{\sigma}(\sigma)] \\ &+[\frac{1}{2}\omega_{\mu}\omega^{\mu} - U_{\omega}(\omega)] \\ &+[\frac{1}{2}\vec{\rho_{\mu}}\Delta\vec{\rho^{\mu}} - U_{\rho}(\rho)] \end{aligned} \tag{2.26}$$

$$\mathcal{H}_{Photon} = \frac{1}{2}A_{\mu}A^{\mu} \tag{2.27}$$

$$\mathcal{H}_{int} = (g_{\sigma}\sigma\bar{\psi}\psi + g_{\omega}\omega_{\mu}\bar{\psi}\gamma^{\mu}\psi + g_{\rho}\vec{\rho_{\mu}}\bar{\psi}\gamma^{\mu}\vec{\tau}\psi + e(\frac{1+\tau_3}{2})A_{\mu}\bar{\psi}\gamma^{\mu}\psi) \tag{2.28}$$

In the Haretree method, the stationary single-nucleon Dirac equation for the nucleons is :

$$\hat{h}_D\psi_i = \epsilon_i\psi_i \tag{2.29}$$

With the Dirac Hamiltonian

$$\hat{h}_D = \alpha(-i\nabla - V(r)) + V_0(r) + \beta(m + S(r)) \tag{2.30}$$

The Hamiltonian contains the attractive scalar field S(r)

$$S(r) = g_\sigma \sigma(r) \tag{2.31}$$

The magnetic potential V(r)

$$V(r) = g_\omega \omega(r) + g_\rho \tau_3 \rho(r) + e\frac{1+\tau_3}{2}A(r) \tag{2.32}$$

And the repulsive time like component of the vector $V_0(r)$

$$V_0(r) = g_\omega \omega_0(r) + g_\rho \tau_3 \rho_0(r) + e\frac{1+\tau_3}{2}A_0(r) \tag{2.33}$$

The corresponding mesons Fields and the electromagnetic field are determined by the Klein-Gordon equations :

$$(-\nabla^2 + m_\sigma^2)\sigma(r) = -g_\sigma \rho_s(r) - g_2\sigma^2(r) - g_3\sigma^3(r) \tag{2.34}$$

$$(-\nabla^2 + m_\omega^2)\omega_0(r) = g_\omega \rho_\nu \tag{2.35}$$

$$(-\nabla^2 + m_\omega^2)\omega_\mu(r) = g_\omega j_\mu \tag{2.36}$$

$$(-\nabla^2 + m_\rho^2)\rho_0(r) = g_\rho \rho_3 \tag{2.37}$$

$$(-\nabla^2 + m_\rho^2)\vec{\rho}_\mu(r) = g_\rho \vec{j}_\mu \tag{2.38}$$

$$-\nabla^2 A_0(r) = e\rho_p(r) \tag{2.39}$$

$$-\nabla^2 A_\mu(r) = e\rho_\mu^p(r) \tag{2.40}$$

The source terms (nuclear currents and densities) appearing in the above equations are :

The scalar density

$$\rho_s(r) = \sum_{i=1}^{A} \bar{\psi}_i(r)\psi_i(r) \tag{2.41}$$

The baryon density

$$\rho_\nu(r) = \sum_{i=1}^{A} \psi_i^+(r)\psi_i(r) \tag{2.42}$$

The isovector density

$$\rho_3(r) = \sum_{i=1}^{A} \psi_i^+(r)\tau_3\psi_i(r) \tag{2.43}$$

The charge density

$$\rho_p(r) = \sum_{i=1}^{A} \psi_i^+(r)(\frac{1+\tau_3}{2})\psi_i(r) \tag{2.44}$$

The baryon current

$$j_\mu(r) = \sum_{i=1}^{A} \bar{\psi}_i(r)\gamma_\mu\psi_i(r) \tag{2.45}$$

The isocurrent

$$\vec{j}_\mu(r) = \sum_{i=1}^{A} \bar{\psi}_i(r)\gamma_\mu\vec{\tau}\psi_i(r) \tag{2.46}$$

To simplify the resulting equations of motion, time reversal symmetry is imposed. This makes the space like components of the fields disappear, and thus there are no currents. Due to charge conservation, only the 3-component of the isovector ρ survives [44].

For the ω meson, the interaction is attractive for all combinations (pp, nn, pn), and for ρ mesons it is attractive for pp and nn currents, but repulsive for pn currents [35].

The occupation probabilities n_i for the state i, in the absence of pairing is given by :

$$\begin{aligned} n_i &= 1, \epsilon_i \leq \epsilon_f \\ &= 0, \epsilon_i > \epsilon_f \end{aligned} \tag{2.47}$$

Here, ϵ_i is the single particle energy of the state i, and ϵ_f is the Fermi energy.

The resulting total energy is then given by

$$\begin{aligned} E[\psi_i, \bar{\psi}_i, \sigma, \omega^0, \rho_3^0, A^0] &= \int \partial^3 r \mathcal{H}(r) \\ &= \sum_{i=1}^{A} \int \partial^3 r \psi_i^+ (-i\alpha\nabla + \beta m)\psi_i \\ +\frac{1}{2}\int \partial^3 r((\nabla\sigma)^2 + U(\sigma)) &- \frac{1}{2}\int \partial^3 r((\nabla\omega^0)^2 + m_\omega^2 \omega^{0^2}) \\ -\frac{1}{2}\int \partial^3 r((\nabla\rho^0)^2 + m_\rho^2 \rho_3^{0^2}) &- \frac{1}{2}\int \partial^3 r(\nabla A^0)^2 \\ + \int \partial^3 r(g_\sigma \rho_s \sigma + g_\omega \rho_\nu \omega^0 + g_\rho \rho_3 \rho_3^0 + e\rho_p A^0) \end{aligned} \tag{2.48}$$

Using the Klein-Gordon equations Eqs.2.34,2.35,2.37,2.39 we obtain the total energy

$$E = \sum_{i=1}^{A} \epsilon_i - \frac{1}{2}\int \partial^3 r(g_\sigma \rho_s \sigma + \frac{1}{3} g_2 \sigma^3 + \frac{1}{2} g_3 \sigma^4 + g_\omega \rho_\nu \omega^0 + g_\rho \rho_3 \rho_3^0 + e\rho_p A^0) \tag{2.49}$$

2.5 Pairing correlations

The Pairing correlations was first investigated by Cooper et al. for infinite nuclear matter, using BCS approach [45]. The BCS model then has been successfully applied in nuclear structure, with mean field models such as Skyrme-HF, Hartree-Fock-Bogoliubov [46] and Relativistic Mean Field [38]. According to the shell model, the energy states are grouped into different shells and there is a large separation between these shells. Nuclei with closed shells are having magic number of protons and neutrons. Pairing correlations involve the formation of proton-proton (pp), neutron-neutron (nn) and proton-neutron (pn) pairs. The last correlations are important in nuclei with the protons and neutron moving in the same open shell. The BCS model is formulated in terms of the Bogoliubov quasiparticles defined as

$$\alpha_k = \sum_n U_{nk} C_n^+ + V_{nk} C_n \tag{2.50}$$

The quasiparticle operators α_k, α_k^+ is the single-nucleons creation and annihilation operators. U,V are the Hartree-Bogoluibove wave function determined by variational method, and n is the index refers to original basis.

Within relativistic Hartree-Bogoliubov (RHB) theory, pairing correlations are described by a density functional

$$E_{RHB}[\hat{\rho},\hat{k}] = E_{RMF}[\hat{\rho}] + E_{pair}[\hat{k}] \tag{2.51}$$

$\hat{\rho}$ is the relativistic single particle dentiy matrix $\hat{\rho}$ and $\hat{k}$ is the pairing-density

$$\rho_{nn'} =< \phi|C_n^+ C_n|\phi > \tag{2.52}$$

$$k_{nn'} =< \phi|C_n C_n|\phi > \tag{2.53}$$

Where $|\phi >$ is the Slater determinate represents the vacuum with quasiparticle. The RMF density functional $E_{RMF}[\hat{\rho}]$ is

$$E_{RMF} = \sum_{i=1}^{A} \int d^3r \psi_i^+(\alpha p + \beta m) - \frac{1}{2}(\nabla A)^2 +$$
$$\frac{1}{2}e \int d^3r j_p^\mu A_\mu + \frac{1}{2}\int d^3r[\alpha_s \rho_s^2 + \alpha_\nu j_\mu j^\mu + \alpha_{TV}\vec{j_\mu} \cdot \vec{j^\mu} + \delta\rho_s\rho_s] \tag{2.54}$$

And the pairing energy $E_{pair}[\hat{k}]$ is

$$E_{pair}[\hat{k}] = \frac{1}{4}\sum_{n_1 n_1{}'}\sum_{n_2 n_2{}'} k_{n_1 n_1'} < n_1 n_1{}'|V^{PP}|n_2 n_2{}' > k_{n_2 n_2'} \tag{2.55}$$

where $< n_1 n_1'|V^{PP}|n_2 n_2' >$ is the matrix element of the two body interaction.

$$V^{pp}(r_1, r_2, r_1', r_2') = -G\delta(R - R')P(r)P(r') \tag{2.56}$$

$$R = \frac{1}{\sqrt{2}}(r_1 + r_2) \tag{2.57}$$

$$r = \frac{1}{\sqrt{2}}(r_1 - r_2) \tag{2.58}$$

$$P(r) = (\frac{1}{4\pi a^2})^{3/2} \exp \frac{-r^2}{2a^2} \tag{2.59}$$

The RHB-coefficients U and V are obtained by the variational :

$$\begin{bmatrix} h_D - M - \lambda & \Delta \\ -\Delta^* & -h_D + M + \lambda \end{bmatrix} \begin{bmatrix} U_k \\ V_k \end{bmatrix} = E_k \begin{bmatrix} U_k \\ V_k \end{bmatrix} \tag{2.60}$$

h_D is the single-nucleon Dirac Hamiltonian given in Eq.(2.29), λ is the chemical potential determined by the average particle number, M is the nucleons mass, and Δ is the pairing field

$$\Delta_{n_1 n_1^{'}} = \frac{1}{2} \sum_{n_2 n_2^{'}} < n_1 n_1^{'} | V^{PP} | n_2 n_2^{'} > k_{n_2 n_2^{'}} \tag{2.61}$$

E_k is the quasiparticle energy , and $\begin{bmatrix} U_K \\ V_K \end{bmatrix}$ is the corresponding eignvector.

2.6 Nuclear deformations

The deformation of the ground state(the nuclear shape), is one of the fundemental properties of an atomic nucleus, along with its mass and radius.

Beginning from the ground-state nuclear shape, a nucleus can take different shapes; spherical, quadrupole (prolate, oblate), and higher order multipole deformed shapes are all possible [23, 47], even though the quadrupole deformed shapes are mostly discussed. The coexistence of different shapes at the same spin and energies is also possible [48, 49]. Coulomb repulsion between protons, the shell structure of nuclei and and pairing correlation are all responsible for the variety of nuclear shapes.

Nuclear deformation is expressed in terms of the shape parameters $\alpha_{\lambda\mu}$ and spherical harmonics $Y_{\lambda\mu}(\theta,\phi)$ as :

$$\mathcal{R}(\theta,\phi) = R_\alpha[1 + \sum_\lambda \sum_{\mu=-\lambda}^{\lambda} \alpha_{\lambda\mu} Y_{\lambda\mu}(\theta,\phi)] \tag{2.62}$$

Where $R(\theta,\phi)$ is the distance of the nuclear surface at (θ, ϕ) from the centre and R_α is the deformation-dependent radius. R_α related to the spherical counterpart R_0 by the condition of volume conservation

$$\frac{4\pi}{3}R_0^3 = \int d\Omega \int^{R(\theta,\phi)} r^2 dr = \frac{4\pi}{3}R_\alpha^3(1 + \frac{3}{4\pi}\sum |\alpha_{\lambda\mu}|^2 + O(\alpha^3)) \tag{2.63}$$

For each mode of order λ, μ has $(2\lambda + 1)$ values; from $-\lambda$ to $+\lambda$. $(\lambda = 0)$, gives the monopole, $\lambda = 1$ corresponds to dipole deformation, $(\lambda = 2)$ to quadrupole deformation and $\lambda = 3$ to octupole deformation. In our calculations, we restrict ourselves to quadruple deformations. For quadrupole shapes,

$$\mathcal{R}(\theta, \phi) = R_\alpha[1 + \sum_\mu \alpha_{2\mu} Y_{2\mu}(\theta, \phi)] \tag{2.64}$$

The quadruple-deformed nuclei are classified into prolate, oblate and triaxial. For such nuclei, with elliptical shape, we can distinguish a coordinate frame defined by the three axes of deformation. Prolate and oblate nuclei are axially symmetric. If the third axis of the nucleus is longer than the others, the nucleus is prolate and if it is shorter, the nucleus is oblate. For triaxial nuclei, the three axes are different[50].

The nuclear deformation is characterized by the deformation parameter β and the triaxiality γ. The five parameters $\alpha_{\lambda\mu}$ can now be reduced to two real parameters α_{20}, α_{22}. We defined Hill-Wheeler coordinate in terms of α_{20} and α_{22} as [51]

$$\alpha_{20} = \beta \cdot \cos\gamma \tag{2.65}$$

$$\alpha_{22} = \frac{1}{\sqrt{2}}\beta \cdot \sin\gamma \tag{2.66}$$

So that

$$\sum |\alpha_{2\mu}|^2 = (\beta)$$

We can connect the quadrupole constraint with β, γ

$$\beta = \sqrt{\frac{4\pi}{5}}\frac{Q}{r^2} \quad , Q = \sqrt{Q_{20}^2 + Q_{22}^2} \tag{2.68}$$

where

$$\hat{Q}_{20} = 2z^2 - x^2 - y^2 \tag{2.69}$$

$$\hat{Q}_{22} = x^2 - y^2 \tag{2.70}$$

$$\gamma = tan^{-1}(\frac{Q_{22}}{Q_{20}}) \tag{2.71}$$

Substituting Eqs .(2.65), (2.66) in Eq .(2.64), we obtain :

$$\mathcal{R}(\theta, \phi) = R_\alpha[1 + \beta\sqrt{\frac{5}{16\pi}}(\cos\gamma(3\cos^2\theta - 1) + \sqrt{3}\sin\gamma\sin^2\theta\cos 2\phi)] \tag{2.72}$$

Then we can calculate the increments of the three semi-axes as a function of β and γ

$$R_x = R(\frac{\pi}{2}, 0) = R_\alpha \cdot [1 + \beta \cdot \sqrt{\frac{5}{4\pi}} \cdot \cos(\gamma - \frac{2\pi}{3})] \tag{2.73}$$

$$R_y = R(\frac{\pi}{2}, \frac{\pi}{2}) = R_\alpha \cdot [1 + \beta \cdot \sqrt{\frac{5}{4\pi}} \cdot \cos(\gamma + \frac{2\pi}{3})] \tag{2.74}$$

$$R_z = R(0, 0) = R_\alpha \cdot [1 + \beta \cdot \sqrt{\frac{5}{4\pi}} \cdot \cos(\gamma)] \tag{2.75}$$

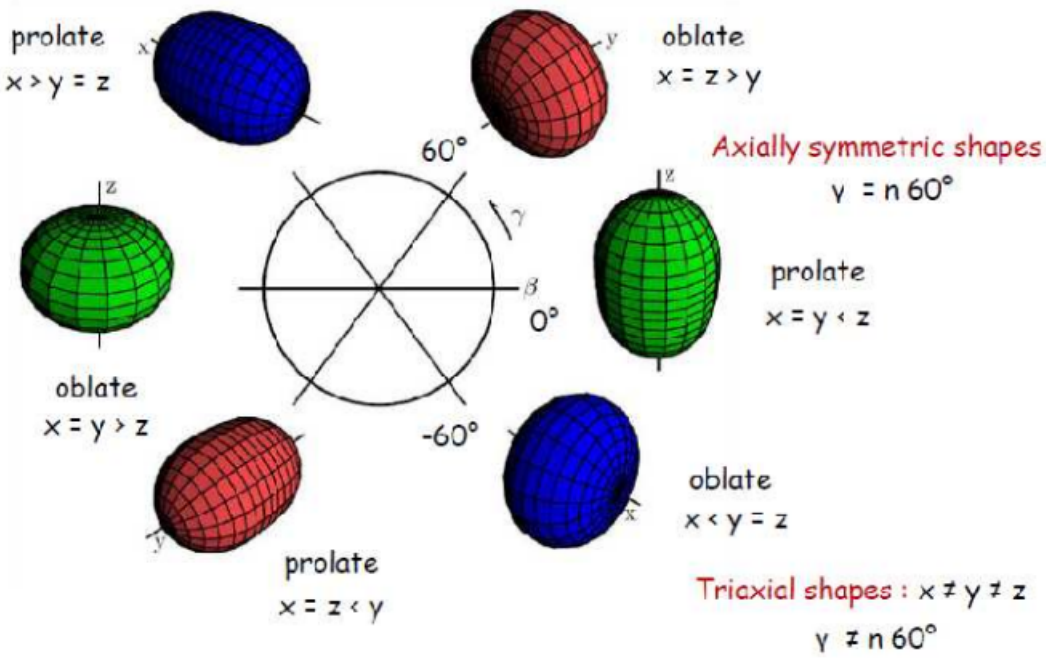

FIGURE 2.1: Variation of nuclear shapes with deformation and triaxiality parameters.

The variation of nuclear shapes with β and γ is illustrated in Fig.2.1 [50]. In general if γ is a multiple of 60° then the shape is axial, and it is triaxial for all other γ values [52, 53]. $\gamma = 0$ and 60° represent prolate and oblate shapes respectively. When γ is a multiple of 60° then the radius along two of the three axis in Eqs.(2.73), (2.74), (2.75) are equal. As we can see:

If $\gamma = 0$, the symmetry axis is Z axis, and $R_x = R_y$.

If $\gamma = 60$, the symmetry axis is Y axis, and $R_x = R_z$.

If $\gamma = 120$, the symmetry axis is X axis, and $R_y = R_z$.

In our calculations of fission barriers, we calculate the nuclear potential energy as a function of deformation paremetr β_2. Positive and negative quadrupole deformations β_2 correspond to prolate (elongated shape) and oblate (flattened shape) respectively.

2.7 The axially symmetric case

For the axially symmetric deformed shape, the rotational symmetry is lost, and thus, the total angular momentum j is not the good quantum number. However, the densities are still invariant with respect to a rotation around the symmetry axis, which is taken to be the z-axis. Hence it is more suitable to use the cylindrical coordinates [54]. For such nuclei, the Dirac spinor ψ_i is now characterized by the quantum numbers (Ω_i, p_i, t_i).

Ω_i is the eigenvalue of the symmetry operator j_{zi}, (j_{zi} is the projection of the single particle angular momentum j_i on the z-axis), p_i is the parity, and t_i is the z-component of the isospin.

The solution of the CDFT equations, and thus the nuclear energy for any point, are determined from the potential energy curves "PEC". The calculations are performed by the method of quadratic constraints [55], which imposed constraints on mass quadrupole moment.

We impose axially symmetric configurations with reflection symmetry, we use the

computer code DIZ [54], based on an expansion of the Dirac spinors in terms of harmonic oscillator wave functions with cylindrical symmetry and we minimize

$$\langle \hat{H} \rangle + C_{20}(\langle \hat{Q}_{20} \rangle - q_{20})^2 \tag{2.76}$$

where $\langle \hat{H} \rangle$ is the total energy, $\langle \hat{Q_{20}} \rangle$ denotes the expectation values of mass quadrupole operators,

$$\hat{Q}_{20} = 2z^2 - x^2 - y^2 \tag{2.77}$$

q_{20} is the constrained value of the multipole moment and C_{20} is the corresponding stiffness constant.

Chapter 3

Fission-Barriers In Pre-Actinide Nuclei

In this chapter we will apply constrained calculation to obtain potential energy curves in the pre-actinide region of nuclear chart. Namely, it will be applied to the even-even nuclei with proton number $80 \leq Z \leq 86$ and $94 \leq N \leq 148$. We are mainly interested in the nuclei with available experimental data or theoretical predictions from different models.

In fission process, a nucleus deviates from its ground-state shape and become more elongated (deformed). The nucleus need to penetrate the barrier, and reach the so-called scission point to separate into two fragments. The height of the fission barrier B_f of a such nucleus, is a measure of its stability and survival probability, reflected in the fission lifetimes of this nucleus .

To evaluate B_f, we calculate the total nuclear potential energy (E) for different nuclear shapes, the potential energy curves (PEC). We restrict ourselves to axially symmetrical deformations with quadrupole degrees of freedom. The saddle-point

and ground-state energies are determined from PEC, defined by the deformation paremeter β_2. For all nuclei under investigation, we carry out calculations of fission barriers using NL3*, DD-ME2, and DD-PC1 parameterizations, with constraints on axial mass quadrupole moment Eq.(2.68). In these calculations, the values of β_2 vary from -0.65 to 1 in steps of 0.05.

3.1 Mercury ($_{80}$Hg) isotopes

3.1.1 Potential energy curves

A systematic calculation of even-even Hg will be performed. It will cover ($94 \leq N \leq 142$) isotopes, for each nucleus, we first calculate the potential energy as a function of the β_2-deformation. Potential energy curves (PEC) are shown in Figs.3.1-3.5 in the three parametrizations, for all of Hg isotopes under study. Energy is shown in these figures are relative energy to the ground state minimum, that is the ground state energy will be zero MeV. Here we will discuss NL3* results, since similar results have been obtained in other parametrizations calculations.

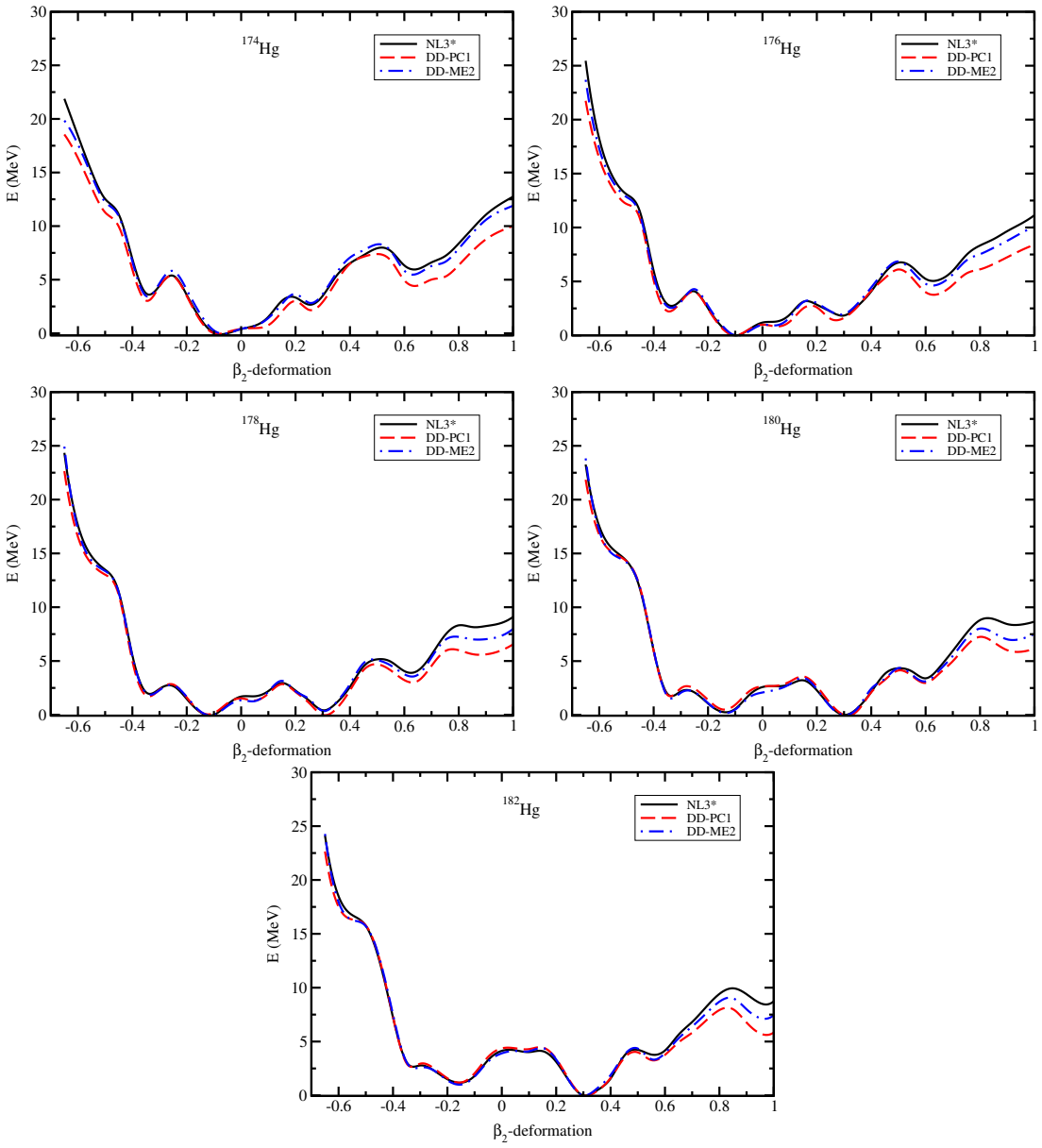

FIGURE 3.1: Potential energy curves of even-even Hg isotopes for neutron number $94 \leq N \leq 102$ as functions of the quadrupole deformation, obtained from an axial RHB calculations with quadratic constraints. Three classes of CDFT models are used, NL3*, DD-ME2, and DD-PC1. The curves are scaled such that the ground state has a zero MeV energy

On the one hand, a single barrier is observed, at β_2= 0.5 in ^{174,176}Hg. On the other hand, a double-humped barrier is observed in ^{178,180,182}Hg. The inner barrier is located at β_2=0.5, in the three isotopes, while the outer one is located at β_2=0.8 in ^{178}Hg, and at β_2=0.85 in ^{180,182}Hg, as shown in Fig.3.1.

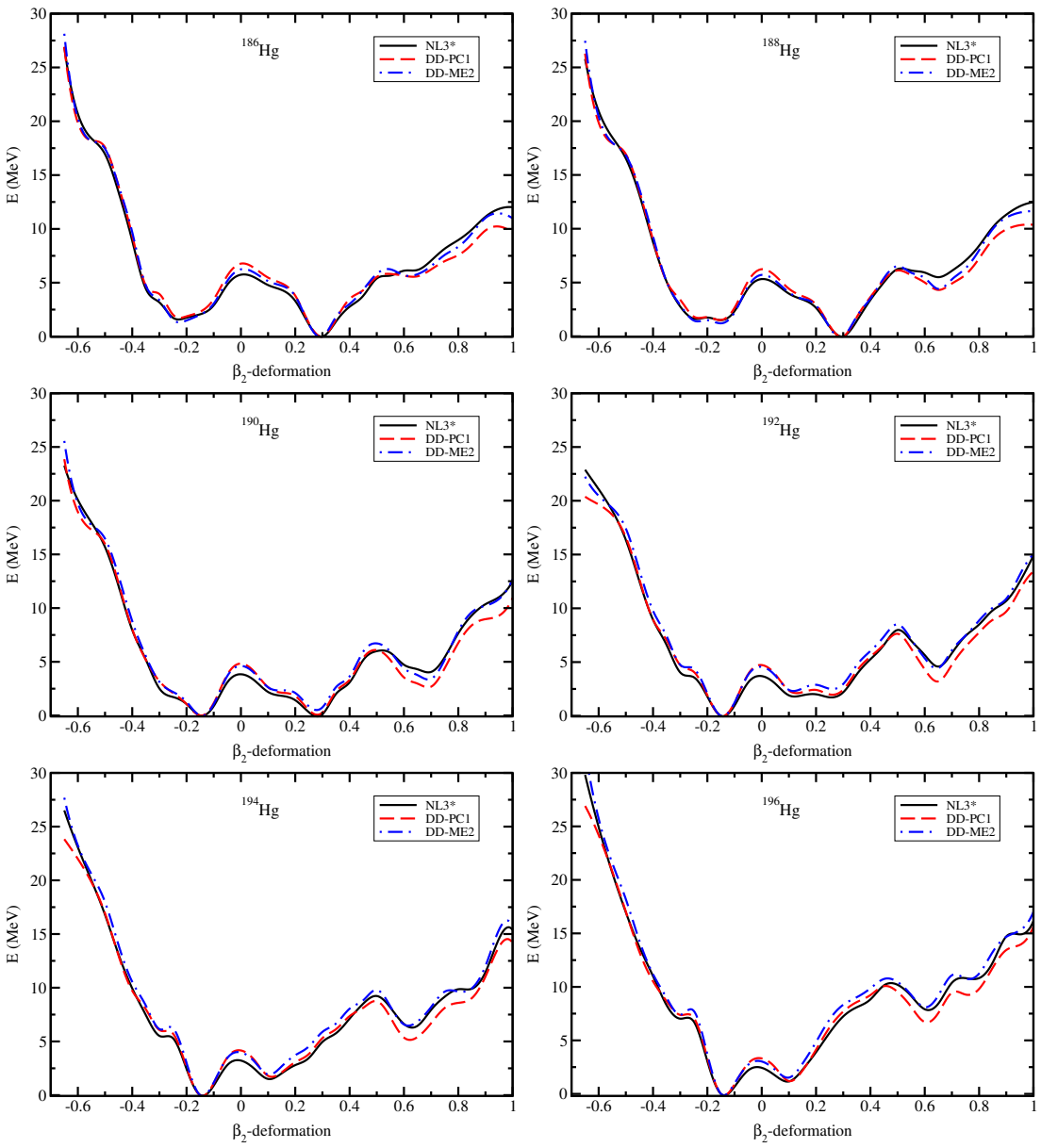

FIGURE 3.2: Same as Fig.3.1, but for $106 \leq N \leq 116$

The second barrier then disappear, and we end up with a single barrier, in the rest of Hg isotopes as seen in Figs.3.2-3.5. The increase of neutron number up to N=116 leads to the emergence of the saddle point to β_2=0.5-0.55; as seen in Fig.3.2 above.

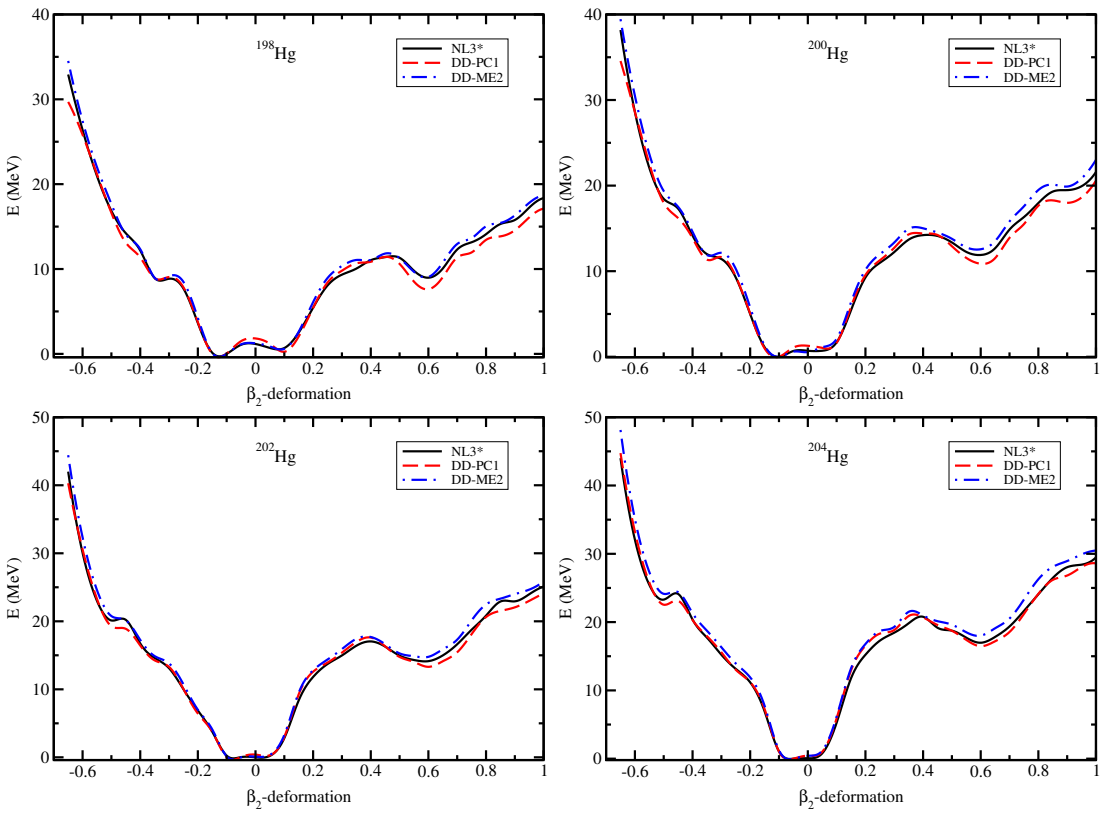

FIGURE 3.3: Same as Fig.3.1, but for $118 \leq N \leq 124$

Obviously, increasing the neutron number beyond $N = 116$ in the nuclei under study, causes the saddle point to be shifted to β_2=0.4-0.45 for $118 \leq N \leq 124$ as it is clearly seen in Fig.3.3. while for the heavier nuclei, in particular, for $126 \leq N \leq 134$, the saddle point emerge to β_2=0.35 as observed in Fig.3.4.

Therefore, it is especially interesting to look for the nucleus ^{216} Hg shown in Fig.3.4. It may however happen that smooth change of the deformation energy curve lead, to the softness of the curve maximum between $\beta_2 = 0.35$ and $\beta_2 = 0.5$.

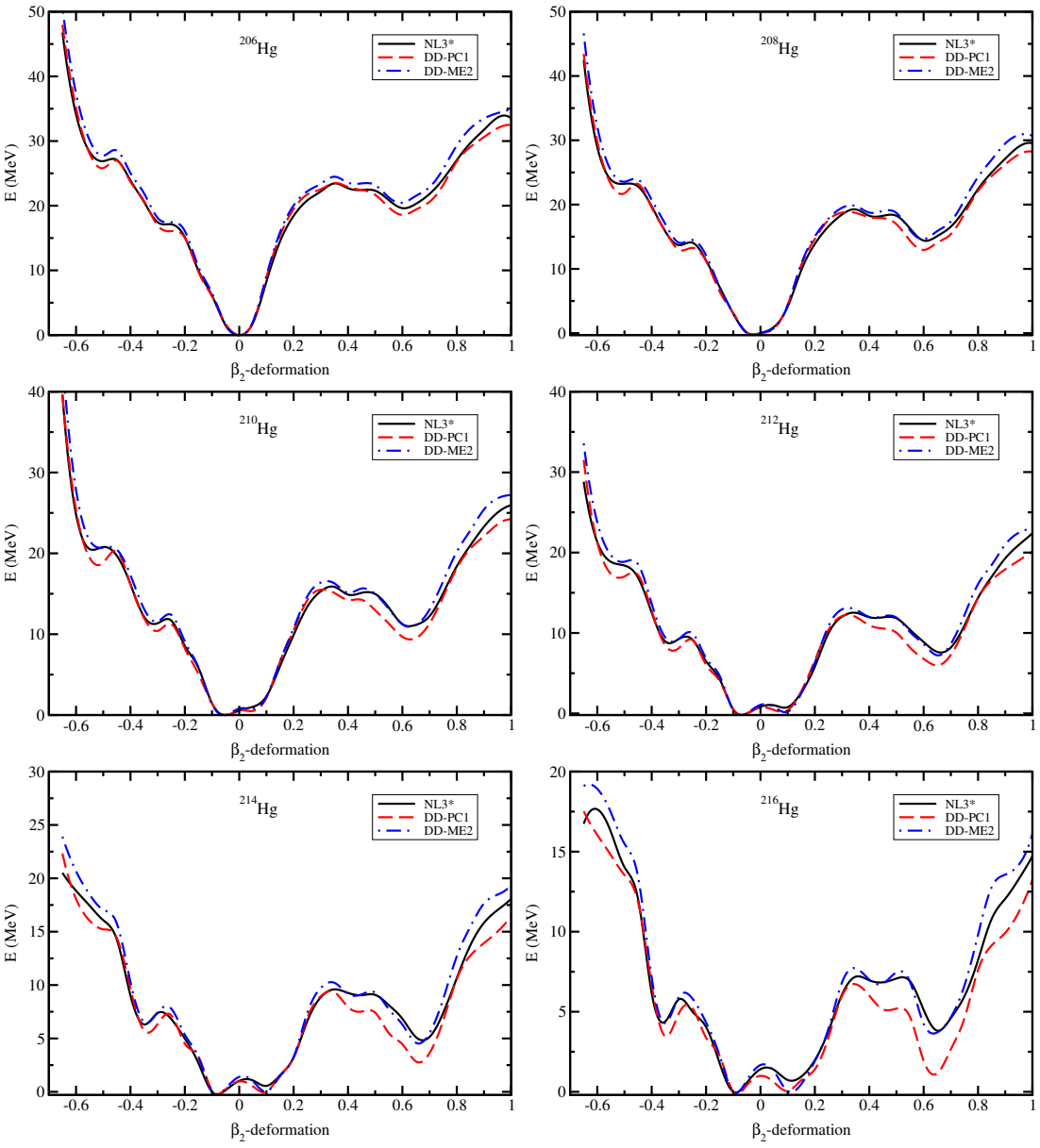

FIGURE 3.4: Same as Fig.3.1, but for $126 \leq N \leq 136$

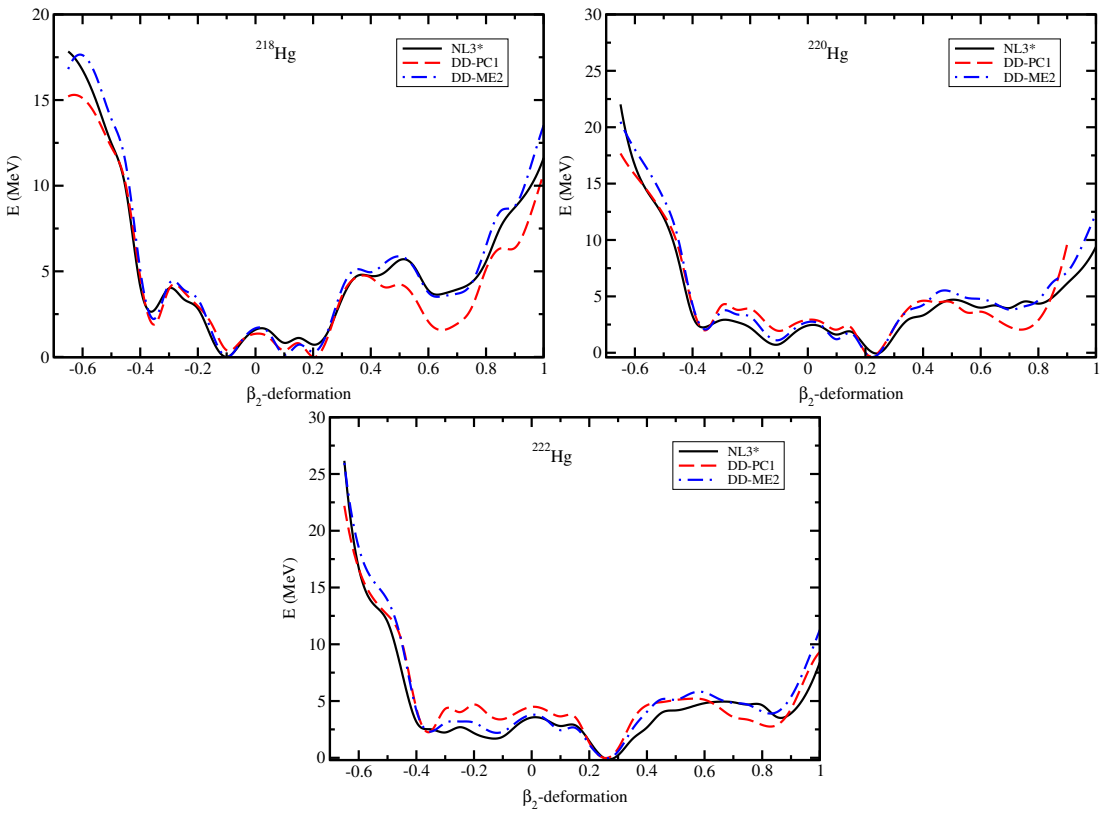

FIGURE 3.5: Same as Fig.3.1, but for $138 \leq N \leq 142$

For the last three nuclei, $138 \leq N \leq 142$, in Fig.3.5, we find out the barrier take place at $\beta_2 = 0.5 - 0.55$, which is similar to the nuclei lying at the beginning of the isotopic chain. The main goal of our present analysis, is to determine the height of such saddle so-called B_f.

3.1.2 Heights of fission barrier

We characterize the fission barrier by a saddle point connecting to pair of minima; The ground-state minimum, and the "fission valley". The heights B_f is defined as the difference between this saddle-point and the ground-state energy. Other

saddle points appear in the potential energy curve, are discarded as being without physical interest.

Our CDFT results for these barriers are presented in Table 3.1 and also in Fig.3.6; the deformation parameters β_2 shown in Table 3.1 are the corresponding elongation parameters.

In the case of more than one barrier observed ($N = 98, 100$ and 102), we consider only the primary barrier (i.e., the highest one). The primary barriers will be generally the better measured than the secondary one (i.e., the lower lying one) Ref.[21]. For these isotopes, it is evident the two barriers are of roughly equal height.

The results of Table 3.1 are displayed in Fig.3.6, where we show the calculated heights of fission barriers as a function of neutron number N, using NL3*, DD-ME2 and DD-PC1. Obviously, among the different classes of CDFT models, the DD-ME2 parametrization always gives the highest values for the fission barrier heights. They are (on average) with difference not exceeding 1.5 MeV, higher than the ones obtained in the NL3* and the DD-PC1 parametrization. It is also obvious from Figs. 3.1-3.6, the heights and the shapes of the fission barriers tend to be very similar for the three parametrizations, especially for the NL3* and the DD-ME2 parametrization.

TABLE 3.1: Calculated fission barrier heights in (MeV) for Hg nuclei, with forces NL3*, DD-PC1 and DD-ME2 within the CDFT framework. ^{i} and ^{o} refer to inner and outer barriers, respectively. Double-humped barriers are predicted for $N = 98, 100$ and 102 only, and no observed barrier for $N = 104$.

		NL3*		**DD-PC1**		**DD-ME2**	
N	A	β_2	B_f	β_2	B_f	β_2	B_f
			Z=80 (Hg)				
94	174	0.5	5.26	0.5	5.21	0.5	5.45
96	176	0.5	4.53	0.5	4.57	0.5	4.88
98	178	0.5^i,0.8^o	4.73^i,4.25^o	0.5^i,0.8^o	4.69^i,2.78^o	0.5^i,0.8^o	4.73^i,3.71^o
100	180	0.5^i,0.85^o	4.33^i,5.50^o	0.5^i,0.8^o	4.13^i,4.28^o	0.5^i,0.8^o	4.35^i,4.90^o
102	182	0.5^i,0.85^o	4.23^i,6.15^o	0.5^i,0.85^o	3.99^i,4.72^o	0.5^i,0.85^o	4.35^i,5.65^o
106	186	0.55	5.82	0.55	5.82	0.55	6.24
108	188	0.5	6.25	0.5	6.12	0.5	6.52
110	190	0.5	5.87	0.5	5.80	0.5	5.95
112	192	0.5	6.26	0.5	5.64	0.5	6.09
114	194	0.5	7.72	0.5	6.94	0.5	7.87
116	196	0.5	9.03	0.45	8.87	0.45	9.21
118	198	0.45	10.71	0.45	11.18	0.45	11.23
120	200	0.4	13.51	0.4	13.36	0.4	14.47
122	202	0.4	17.04	0.4	17.31	0.4	17.59
124	204	0.4	20.78	0.35	20.45	0.35	21.08
126	206	0.35	23.45	0.35	23.51	0.35	24.48
128	208	0.35	19.25	0.3	18.75	0.35	19.73
130	210	0.35	15.30	0.3	14.99	0.3	15.60
132	212	0.35	11.72	0.3	11.70	0.3	12.73
134	214	0.35	9.04	0.35	9.33	0.35	10.19
136	216	0.35-0.5	6.45-6.34	0.35-0.5	6.67-5.15	0.35-0.5	7.67-7.46
138	218	0.5	4.93	0.35	4.64	0.5	5.58
140	220	0.5	4.70	0.4	4.61	0.5	5.40
142	222	0.65	4.94	0.55	5.20	0.6	5.76

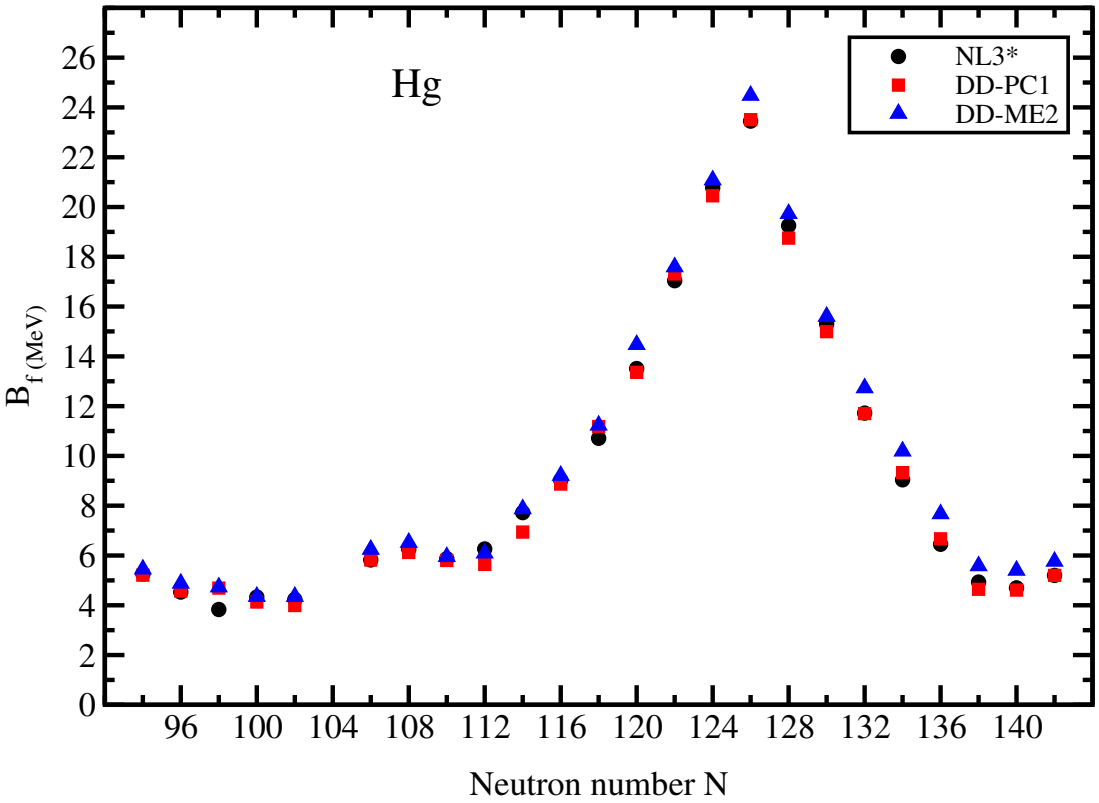

FIGURE 3.6: Fission barrier heights for Hg nuclei as a function of neutron number N, Obtained with the NL3*(black circles), DD-PC1(red squares) and DD-ME2(blue triangles) parametrizations of RMF Lagrangian. (Note that no fission barrier is predicted for N=104)

3.1.3 Comparison with experimental data and other theoretical models

It is interesting now to examine our model by comparing the current results with the experimental ones and the ones obtained in other models. There is only one experimental work Ref.[56], where the authors estimates the heights of fission barriers in the pre-actinide region with $Z = 80, 82, 84$ and 86. Unfortunately, for a given proton number Z, a sequence of at least 20 even-even nuclei is being under the study, such that at most 3 nuclei of this sequence have an experimental value.

In Table 3.2 and also in Fig.3.7, we collect some of the theoretical predictions of fission barrier heights, based on the finite range liquid-drop model (FRLDM)[23], the self-consistent Hartree-Fock (SHF) method[21] with BSK8 Skyrme interaction, the extended Thomas-Fermi Plus Strutinsky integral (ETFSI) model[17, 18] and the results of the LDM calculations within the microscopic-macroscopic method (MM)[4], where present in relation to experimental ones[56].

The comparison of our calculated heights, and those obtained from the FRLDM model, shows that the latter predictions are systematically higher than ours. However, one can see that the two models have the same behavior, as shown in Table 3.2 and Fig.3.7. We find that there is slow but steady increase in the calculated height as N increase, the results show a maximum at ^{206}Hg, and then with increasing N fall to a minimum at around $N = 140$, the value for which this barrier becomes observable. At this point, the barrier height is underestimated by about 4.70 MeV. We can report here that our results are always lower than the FRLDM ones by 10 MeV, for some nuclei (and often much smaller for the majority of nuclei).

Table 3.2: Comparison of fission barrier height from NL3*parametrizations, with other theoretical evaluations: SHF [21], FRLDM [23], ETFSI [17], CDFT (present work), and experimental data taken from Ref.[56], except as indicated in footnote. All quantities are in (MeV), except for numbers specifying the nucleus. Dashes mean not measured or not calculated.

Z	N	A	CDFT	FRLDM	ETFSI	SHF	MM	EXP
80	94	174	5.26	9.63	-	-	-	-
	96	176	4.53	9.62	-	-	-	-
	98	178	3.83	9.32	-	-	-	-
	100	180	4.33	9.81	-	-	-	-
	102	182	4.23	10.85	-	-	-	-
	104	184	-	11.92	-	-	-	-
	106	186	5.82	12.99	-	-	-	-
	108	188	6.25	13.98	-	-	-	-
	110	190	5.87	15.22	-	-	-	-
	112	192	6.26	16.75	-	-	-	-
	114	194	7.72	18.10	-	-	-	-
	116	196	9.03	19.65	-	-	-	16.9
	118	198	10.71	21.45	10.1	9.3	-	16.6,20.4[a]
	120	200	13.51	23.23		-	-	17.7
	122	202	17.04	24.79	-	-	-	-
	124	204	20.78	26.11	-	-	-	-
	126	206	23.45	27.21	-	-	-	-
	128	208	19.25	25.51	-	-	-	-
	130	210	15.30	23.32	-	-	-	-
	132	212	11.72	21.27	-	-	-	-
	134	214	9.04	19.80	-	-	-	-
	136	216	6.45-6.34	18.33	-	-	-	-
	138	218	4.93	17.04	-	-	-	-
	140	220	4.70	15.69	-	-	16.55	-
	142	222	5.20*	14.56	-	-	14.98	-

[a]Moller-2004 [11].

* From DD-PC1 Parametrization.

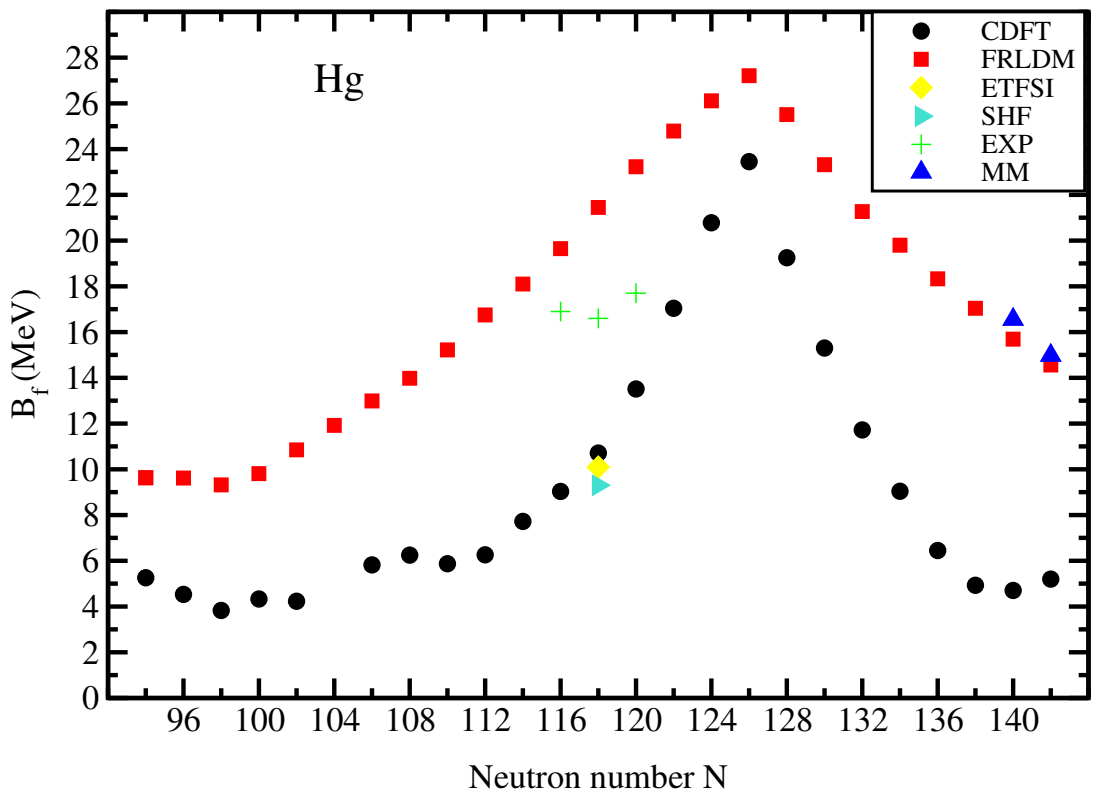

FIGURE 3.7: Comparison of fission barriers as a function of neutron number N, calculated by Moller et al.(FRLDM)(Ref.[23]), Mamdouh et al.(ETFSI)(Ref.[17]), Samyn et al. (SHF)(Ref.[21]), Howard et al.(MM)(Ref.[4]) and by us (CDFT) with experimental data (EXP)(Ref.[56]) (Note that no fission barrier is predicted for $N = 104$ in our model).

Let us re-examine this comparison between the calculated and experimental barrier heights, the solid green plus in Fig.3.7, denote the few experimental barrier heights that have been measured for this isotopic chain. It is evident here that the guess of the same trend existing for the experimental barriers is impossible, due to the narrow experimentally known region. But, in the same time, a glance at Table 3.2 and Fig.3.7 show that the presence of experimental barriers between the values obtained by the two models, gives a good prospective to our results.

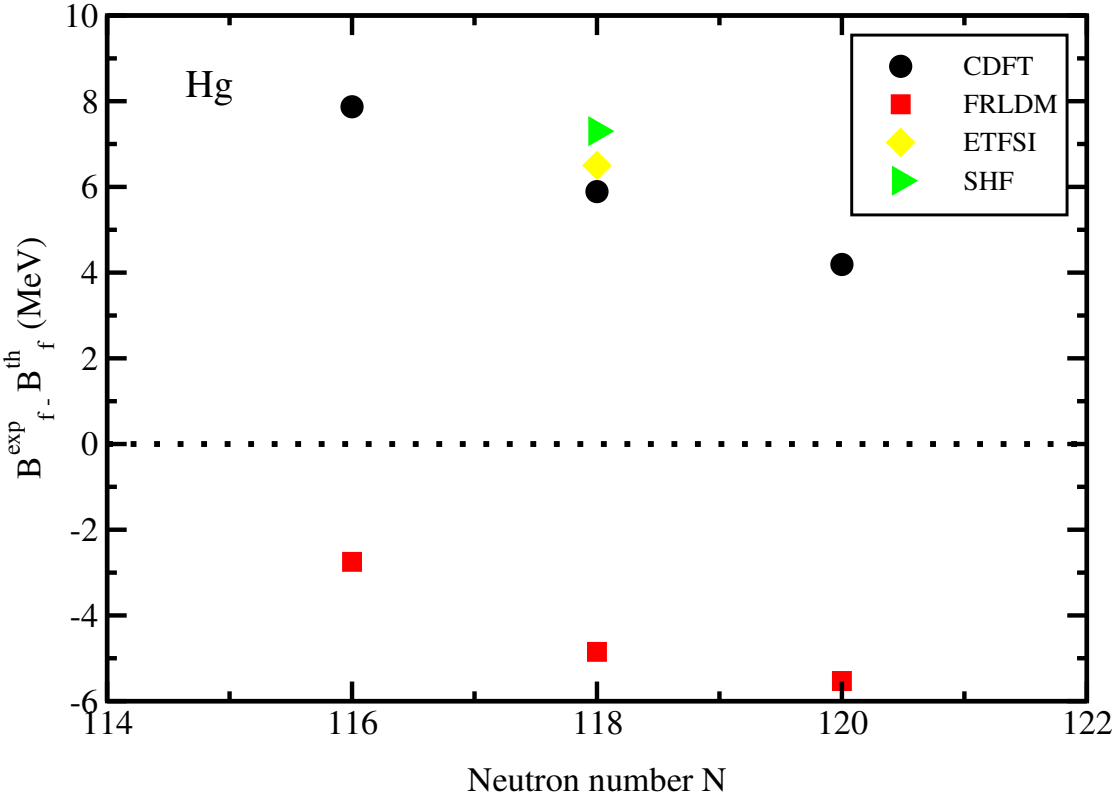

FIGURE 3.8: The difference between experimental and calculated heights of inner fission barriers as a function of neutron number N. The results of the calculations within microscopic-macroscopic method ('SHF(Samyn)' [21]), the finite range liquid-drop model ('FRLDM(Moller)' [23]), the covariant density functional theory ('CDFT') and the extended Thomas-Fermi plus Strutinsky integral ('ETFSI(Mamdouh)' [17]) are shown. .

Turning now to the discrepancies of different presented models values, shown in the Table 3.2 and the Fig.3.7, with the experimental ones [56], the difference between all theoretical calculations and experimental values is shown in Fig.3.8.

As we can see, our calculated barriers are (on average) by 4-8 MeV lower than experimental ones, while FRLDM significantly overestimate the barrier, they are (on average) by 3-6 MeV higher.

We consider now ^{198}Hg nucleus, where three theoretical values other than our value for the barrier height exist, the FRLDM model gives a value of 21.45 MeV, while the value obtained in our approach is 10.71 about 10 MeV lower, whereas the experimental data indicate 16.6 MeV. The ETFSI and SHF models underestimate the value of 10.1 and 9.3 MeV, respectively, the agreement with our value is much better than the one with FRLDM model.

The disagreement with experimental data, shown in Fig.3.7, is not very surprising if one takes into account that experimentally, the fission barrier are not directly measured, and model-dependent analysis is involved to obtain these quantities [22]. Moreover a relatively small number of nuclei are considered here, which limits the comparison. According to the theoretical models, the differences are due to the difference observed in the shape parametrization, and the deformation space used in the calculation.

3.2 Lead ($_{82}$Pb) isotopes

3.2.1 Potential energy curves

Potential energy curves for even-even Pb isotopes with N ranging from 96 to 148, are shown in Figs.3.9-3.14. Since all of the CDFT parametrizations give similar results, only NL3* results will be discussed.

We find ^{178}Pb and ^{180}Pb nuclei to have a double-humped barrier. The first barrier is located at β_2=0.15 for both nuclei, whereas the second one is located at β_2=0.5 for ^{178}Pb and at β_2=0.55 in the case of ^{180}Pb nucleus as shown in Fig.3.9.

It should be noted here that within the CDFT model, using the three parmetrizations, fission barriers are not observed in the PEC for ^{182}Pb, ^{186}Pb and ^{188}Pb, as seen in Fig.3.10.

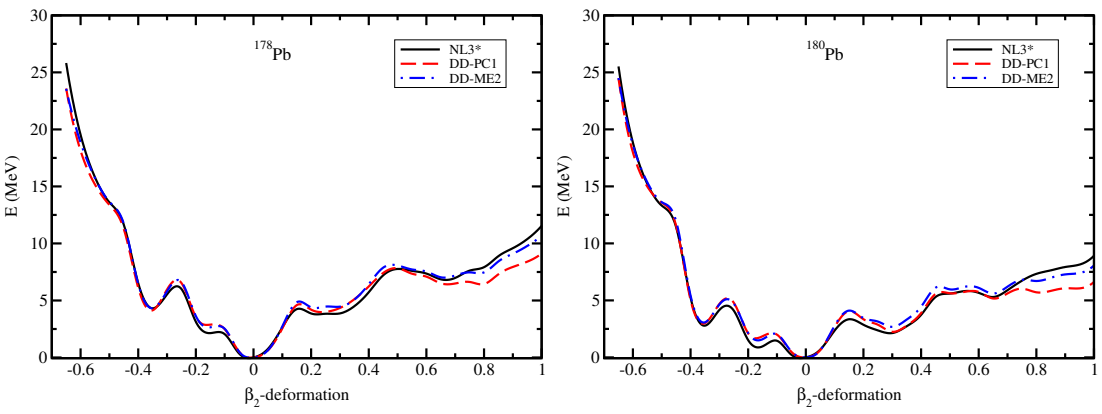

FIGURE 3.9: Potential energy curves for ^{178}Pb and ^{180}Pb nuclei as functions of the quadrupole deformation β_2. The effective interactions used are NL3*, DD-ME2, and DD-PC1. The curves are scaled such that the ground state has a zero MeV energy

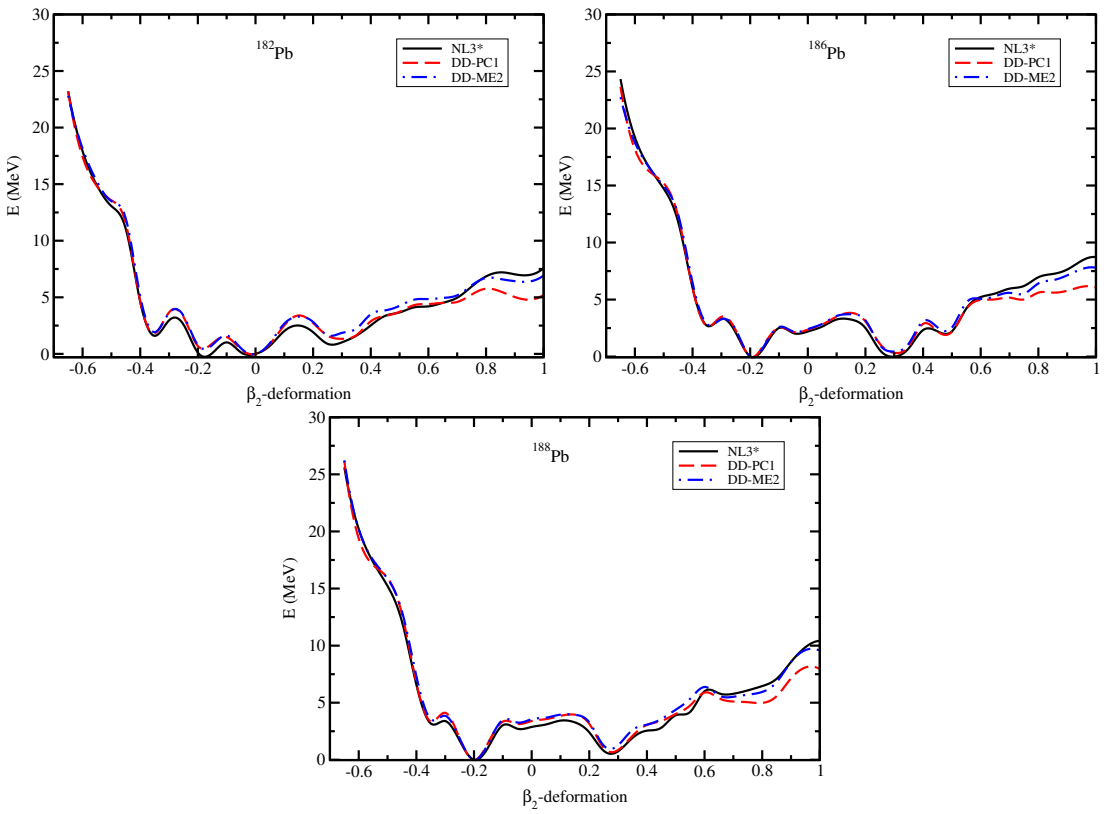

FIGURE 3.10: Same as Fig.3.9, but for $N = 100, 104$ and 106

It is also interesting to notice that when we reach $N = 108$, the barrier is no longer double-humped, this can be seen in Figs.3.11-3.14. In the nuclei with $108 \leq N \leq 112$, the barrier is observed at $\beta_2 = 0.5 - 0.6$, as it is already in Fig.3.11.

Another important observation, in the nuclei under study, concerns the change in the barrier location with the neutron number N. One can notice from Fig.3.12 that the saddle point, for $114 \leq N \leq 122$ arise at $\beta_2 = 0.4 - 0.45$, whereas for the heavier nuclei, in particular for $124 \leq N \leq 140$, the saddle point emerges to $\beta_2 = 0.3 - 0.4$ (i.e., to lower β_2 value), as observed in Fig.3.13.

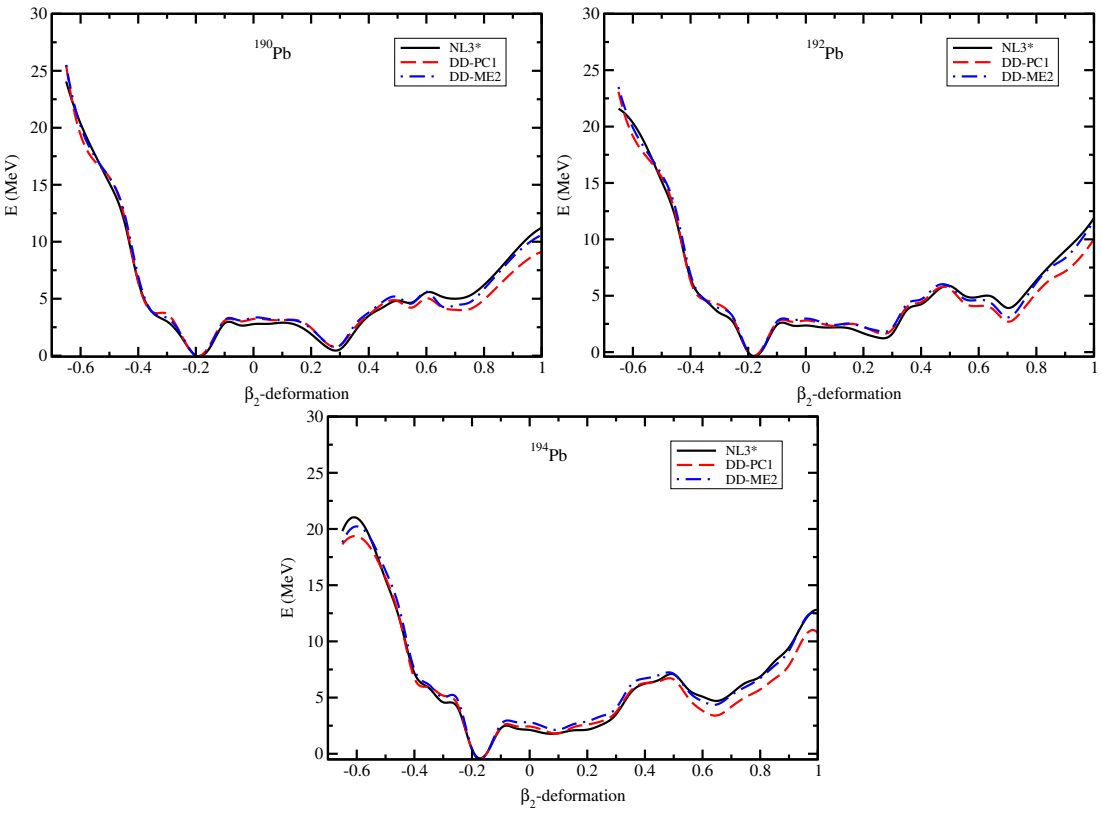

FIGURE 3.11: Same as Fig.3.9, but for $108 \leq N \leq 112$

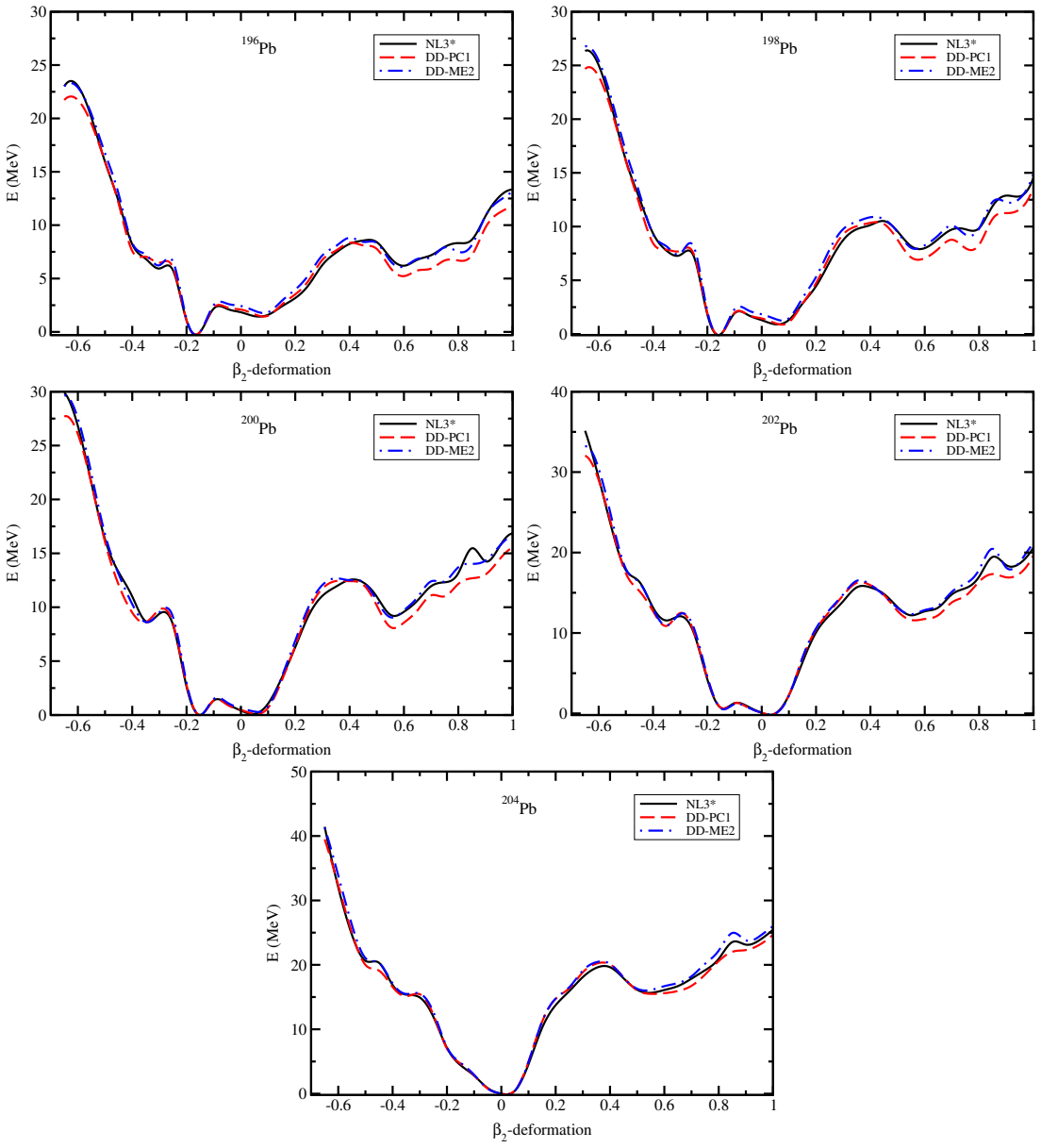

FIGURE 3.12: Same as Fig.3.11, but for $114 \leq N \leq 122$

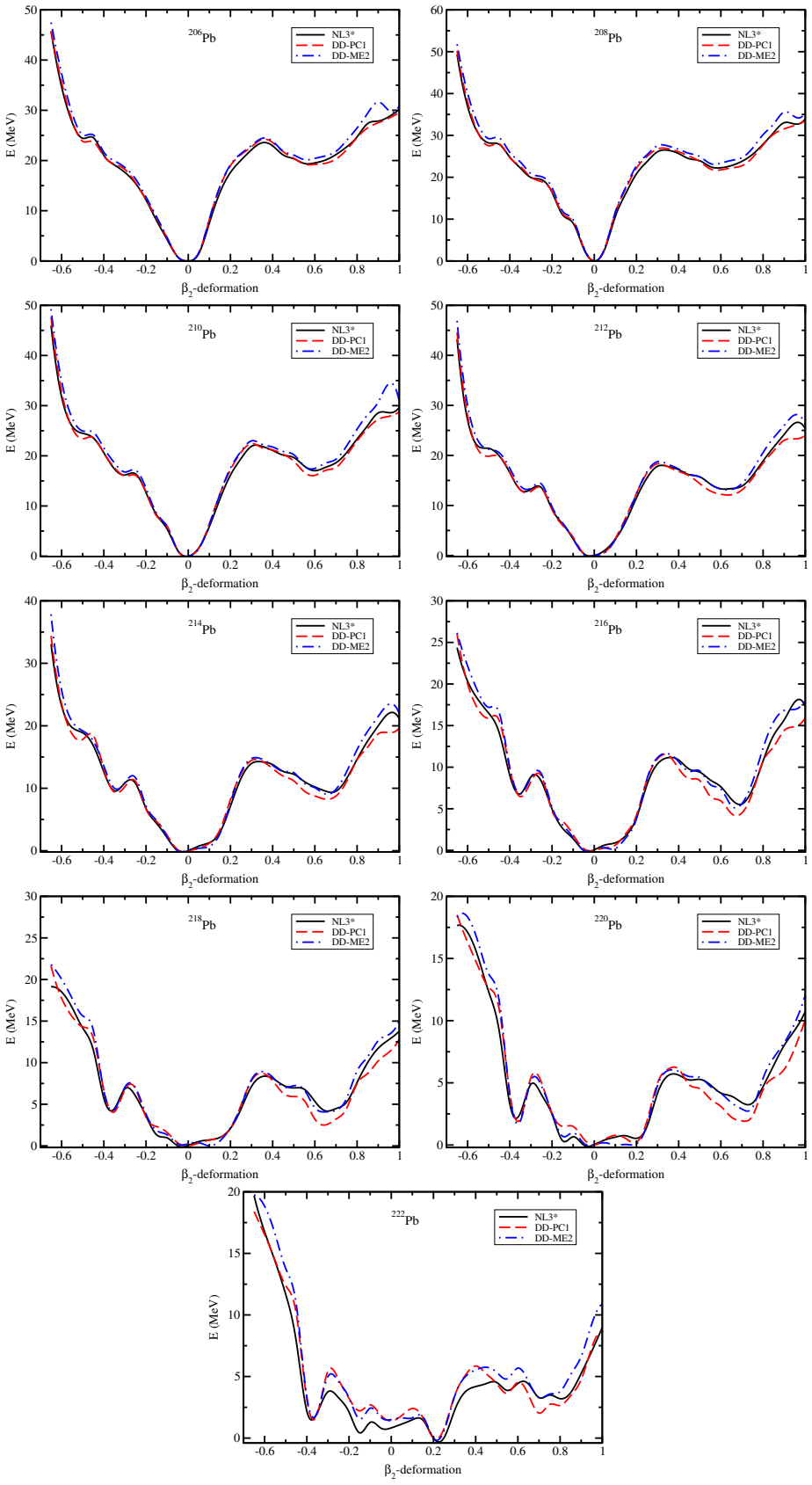

FIGURE 3.13: Same as Fig.3.9, but for $124 \leq N \leq 140$

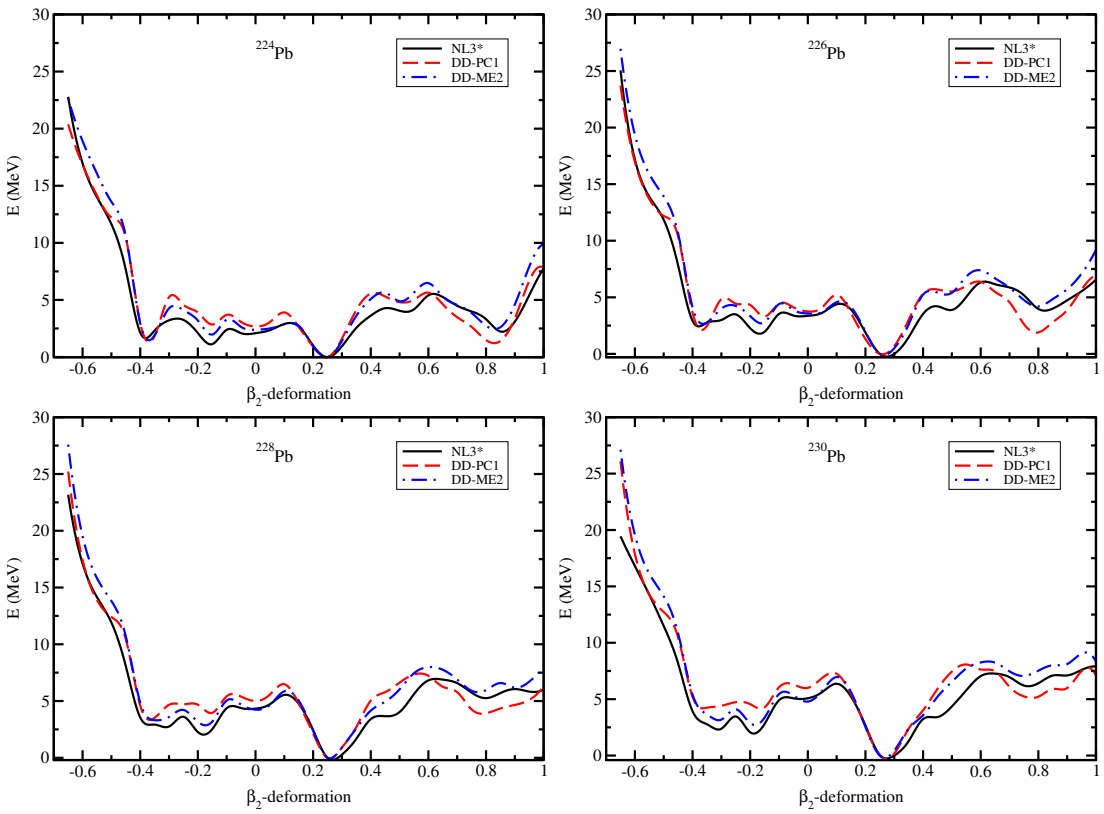

FIGURE 3.14: Same as Fig.3.9, but for $142 \leq N \leq 148$

In $142 \leq N \leq 148$ nuclei, we find the barrier arise again at $\beta_2 = 0.6 - 0.65$ (i.e., at higher deformation), as its visible in Fig.3.14.

3.2.2 Heights of fission barrier

Here, we associate the height with the saddle point B_f, we already have observed via PEC. Whenever we have a double humped barrier, we consider the highest i.e., the primary barrier. The result of these calculations, for NL3*, DD-PC1 and DD-ME2 forces, are given in Table 3.3, which shows for each nucleus, the height of the primary barrier, and in the case of a double barrier, the secondary barrier, with the corresponding deformation parameter β_2.

TABLE 3.3: Calculated fission barrier heights in (MeV) for Pb nuclei, with forces NL3*, DD-PC1 and DD-ME2 within the CDFT framework. ^{i} and ^{o} refer to inner and outer barriers, respectively.

		NL3*		**DD-PC1**		**DD-ME2**	
N	A	β_2	B_f	β_2	B_f	β_2	B_f
			Z=82 (Pb)				
96	178	0.15^i,0.5^o	$4.24^i, 3.90^o$	$0.15^i, 0.5^o$	$4.59^i, 3.82^o$	$0.15^i, 0.5^o$	$4.84^i, 3.67^o$
98	180	$0.15^i, 0.55^o$	$3.34^i, 3.68^o$	$0.15^i, 0.55^o$	$4.06^i, 3.50^o$	$0.15^i, 0.55^o$	$4.19^i, 3.51^o$
108	190	0.6	4.99	0.6	4.13	0.6	4.72
110	192	0.5	4.58	0.5	3.91	0.5	3.91
112	194	0.5	5.23	0.5	4.80	0.5	4.98
114	196	0.45	7.09	0.4	6.82	0.4	6.98
116	198	0.45	9.60	0.4	9.35	0.4	9.47
118	200	0.4	12.43	0.35	12.32	0.35	12.36
120	202	0.4	15.68	0.35	16.23	0.35	16.49
122	204	0.4	19.64	0.35	20.19	0.35	20.42
124	206	0.35	23.53	0.35	24.20	0.35	24.41
126	208	0.35	26.44	0.35	26.81	0.3	27.55
128	210	0.3	21.90	0.3	22.45	0.3	22.98
130	212	0.3	17.84	0.3	18.35	0.3	18.74
132	214	0.35	14.23	0.3	14.47	0.3	14.66
134	216	0.35	11.14	0.35	11.44	0.35	11.47
136	218	0.35	8.33	0.35	8.72	0.35	8.93
138	220	0.4	5.32	0.35	6.11	0.35	5.99
140	222	0.5	4.51	0.4	5.85	0.45	5.75
142	224	0.6	5.41	0.6	5.64	0.6	6.47
144	226	0.6	6.32	0.6	6.37	0.6	7.38
146	228	0.65	6.89	0.55	7.33	0.6	7.99
148	230	0.65	7.27	0.55	8.07	0.6	8.26

Remarkably, the three parametrization predict ^{178}Pb and ^{180}Pb to have a double barrier. A glance at Table 3.3, shows that the two barriers are of roughly equal height. It can be seen also the vanishing of one barrier, and the appearance of a single observed one, as a result of neutron number N increasing. We now recall that such increasing, causes an emergence of this single barrier to different deformation value β_2, of the nuclei in question.

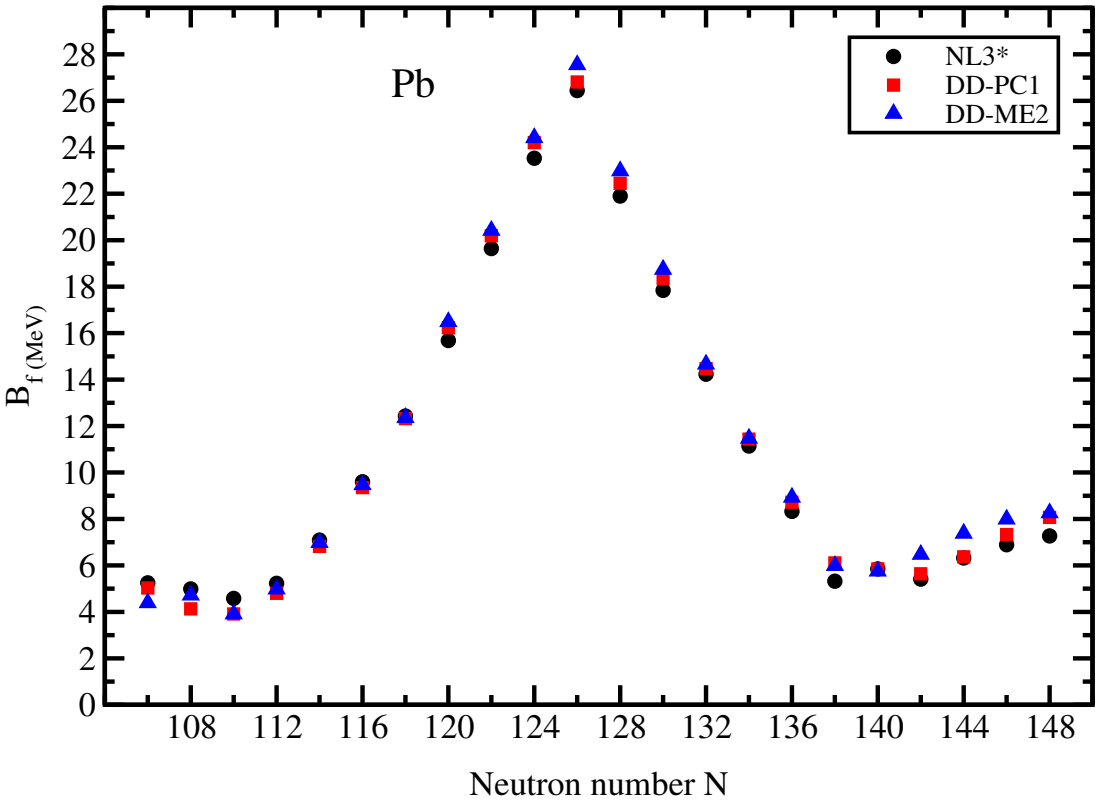

FIGURE 3.15: Fission barrier heights for Pb nuclei as a function of neutron number N, Obtained with the NL3*(black circles), DD-PC1(red squares) and DD-ME2(blue triangles) parametrizations of RMF Lagrangian.

The results of Table 3.3, are displayed in Fig.3.15, where we show the calculated heights of fission barriers, as a function of neutron number N, in three classes of CDFT, as well as we label in Fig.3.15. We emphasize that in our calculations, we obtain barriers of the highest values with DD-ME2 parametrization. They are (on average) with difference not exceeding 1.5 MeV, higher than the ones obtained in the NL3*, and the DD-PC1 parametrization. As mentioned earlier, the PEC in Figs.3.9-3.14 look similar in these parametrizations, and thus, the saddle locations obtained in these calculations, did not exhibit a significant difference, hence, it was safe to take into account the NL3* calculations only, in the preceding subsection.

3.2.3 Comparison with experimental data and other theoretical models

Now, we check whether or not these obtained results, are agreed with the experimental ones, and the ones obtained in other models. Only 3 nuclei in the Pb isotopic chain have an experimental value. Fortunately, there have already been many calculations of the barriers of some particular nuclei. Two systematic calculations has been performed; The 1980 macroscopic-microscopic (MM) calculation of Haward and Moller [4], and the calculation of Moller et al. [23], using the finite-range liquid-drop model (FRLDM), covering all the required nuclei, and casting doubt on all previous MM calculations of barriers.

The two other calculations are microscopic calculation: The self-consistent Hartree-Fock (SHF) [21], and Mamdouh et al. [17], based on the ETFSI (extended Thomas-Fermi plus Strutinsky integral), the later is a high-speed approximation to the Skyrme-HF method [15]. These calculations except the FRLDM one include a few measured nuclei, given in Table 3.4 and Fig.3.16.

Table 3.4: Comparison of fission barrier heights with other theoretical evaluations: SHF [21], FRLDM [23], ETFSI [17], CDFT (present work), and experimental data taken from Ref.[56]. All barriers are from NL3* parametrizations, except as indicated in footnote. All quantities are in (MeV), except for numbers specifying the nucleus. Dashes mean not measured or not calculated.

Z	N	A	CDFT	FRLDM	ETFSI	SHF	MM	EXP
82	96	178	4.24	7.99	-	-	-	-
	98	180	3.34	8.47	-	-	-	-
	100	182	-	8.62	-	-	-	-
	104	186	-	9.61	-	-	-	-
	106	188	-	10.32	-	-	-	-
	108	190	4.99	11.18	-	-	-	-
	110	192	4.58	12.85	-	-	-	-
	112	194	5.23	14.50	-	-	-	-
	114	196	7.09	15.66	-	-	-	-
	116	198	9.60	17.28	-	-	-	-
	118	200	12.43	18.89	-	-	-	-
	120	202	15.68	20.48	-	-	-	-
	122	204	19.64	21.91	15.7	14.3	-	23.5
	124	206	23.53	23.94	17.8	16.5	-	25.3
	126	208	26.44	24.95	19.7	17.0	-	27.4
	128	210	21.9	22.91	-	-	-	-
	130	212	17.84	20.77	-	-	-	-
	132	214	14.23	19.13	-	-	-	-
	134	216	11.14	17.95	-	-	-	-
	136	218	8.33	16.83	-	-	-	-
	138	220	5.32	15.33	-	-	-	-
	140	222	5.85*	13.70	-	-	16.67	-
	142	224	5.41	12.48	-	-	15.04	-
	144	226	6.32	12.34	-	-	13.51	-
	146	228	6.89	12.16	-	-	12.46	-
	148	230	7.27	12.58	-	-	10.16	-

* From DD-PC1 Parametrization.

In order to gain some confidence in our results, we first compare our calculated barriers with those obtained from the FRLDM, it can be seen from Table 3.4, and Fig.3.16 that in the whole region of considered nuclei, the FRLDM barriers are higher than Ours. The agreement become much better in the subsequence $120 \leq N \leq 132$, with difference less than 5 MeV. The same figure shows the behavior of fission barrier heights, with increasing neutron number N, throughout the sequence. One can recognize, the steady increase in barrier height till ^{208}Pb nucleus, where the highest value is obtained, follows by steady decrease till ^{220}Pb nucleus, then the steady increase again at the end of the sequence.

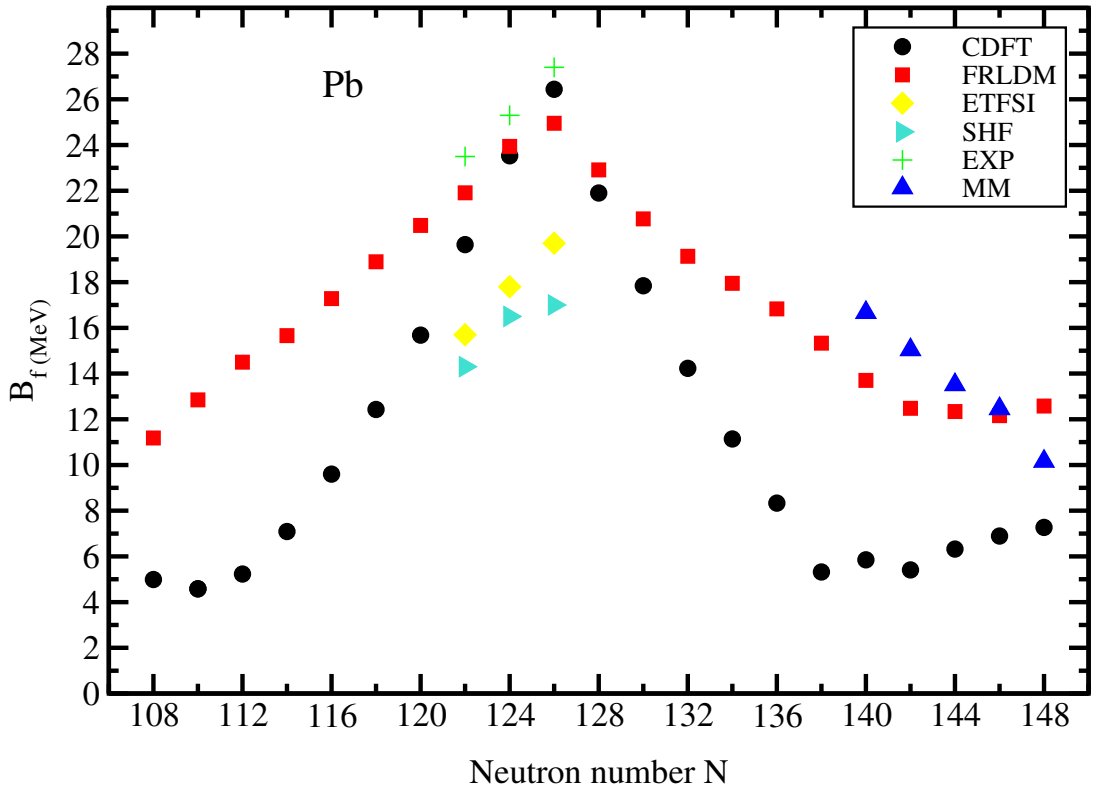

FIGURE 3.16: Comparison of fission barriers as a function of neutron number N, calculated by Moller et al.(FRLDM)(Ref.[23]), Mamdouh et al.(ETFSI)(Ref.[17]), Samyn et al. (SHF)(Ref.[21]), Howard et al.(MM)(Ref.[4]) and by us (CDFT) with experimental data (EXP)(Ref.[56]).

Our calculated values tend to be $1-4$ MeV lower than the experimental values, nothing can be guessed regard the tendency of experimental barriers, due to the lack of abundance of experimental values in the considered region. Note that lower limits for the fission barrier heights are predicted by ETFSI and SHF models, as indicated by the Diamond and right triangle, respectively in Fig.3.16. MM barriers are always higher than ours, for the few cases where these are available, denoted in the same figure by the up triangle.

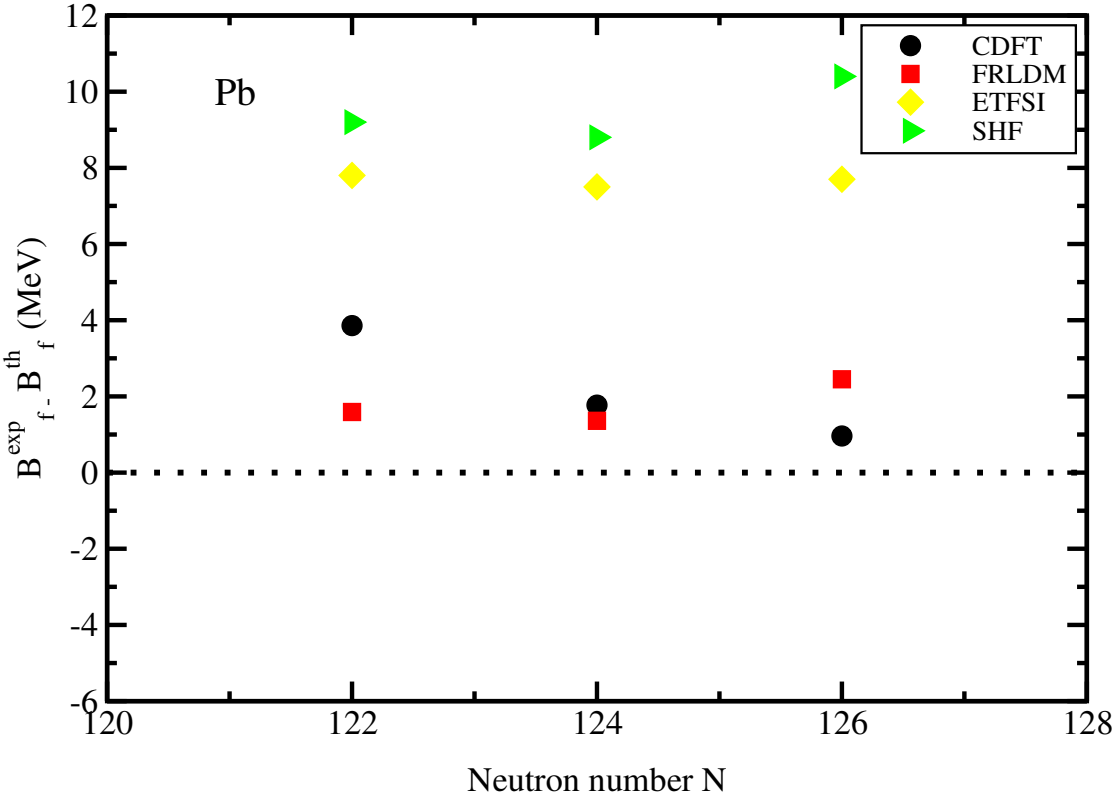

FIGURE 3.17: The difference between experimental and calculated heights of inner fission barriers as a function of neutron number N. The results of the calculations within microscopic-macroscopic method ('SHF(Samyn)' [21]), the finite range liquid-drop model ('FRLDM(Moller)' [23]), the covariant density functional theory ('CDFT') and the extended Thomas-Fermi plus Strutinsky integral ('ETFSI(Mamdouh)'[17]) are shown.

We show in Fig.3.17 the deviation ΔB_f, of some of our calculated barrier heights, from the experimental values; in the same figure, we show also the corresponding quantities for the FRLDM, the ETFSI and the SHF models. Clearly, both ETFSI and SHF significantly underestimate the barrier heights; the deviation from the experimental values is about 8 MeV, in the case of ETFSI results. SHF results are worse than those for the ETFSI ones, with deviation from 9 to 11 MeV, for this group of nuclei. On the other hand, calculations based on the FRLDM predict the barriers to be 1-3 MeV lower, but the agreement is, however, much better.

3.3 Polonium ($_{84}$Po) isotopes

3.3.1 Potential energy curves

In Figs.3.18-3.20 PEC for Po isotopes are given. Such curves enabled us to find, the saddle point location and energy.

Po isotopes, beginning with $A = 186$ up to $A = 230$, exhibit a single barrier at relatively high deformation, The β_2 values are hung about 0.65-0.7, as observed in Fig.3.18.

In Fig.3.19, PEC of Po nuclei with N ranging from 112 to 140 are presented. It is seen that as we go from the lighter isotopes to the heavier ones, the saddle point change its position to lower deformations. That is, the lighter isotopes need higher deformation to undergoes a fission. For this subset of the considered nuclei, the β_2 values fluctuate between 0.3, 0.35 and 0.4.

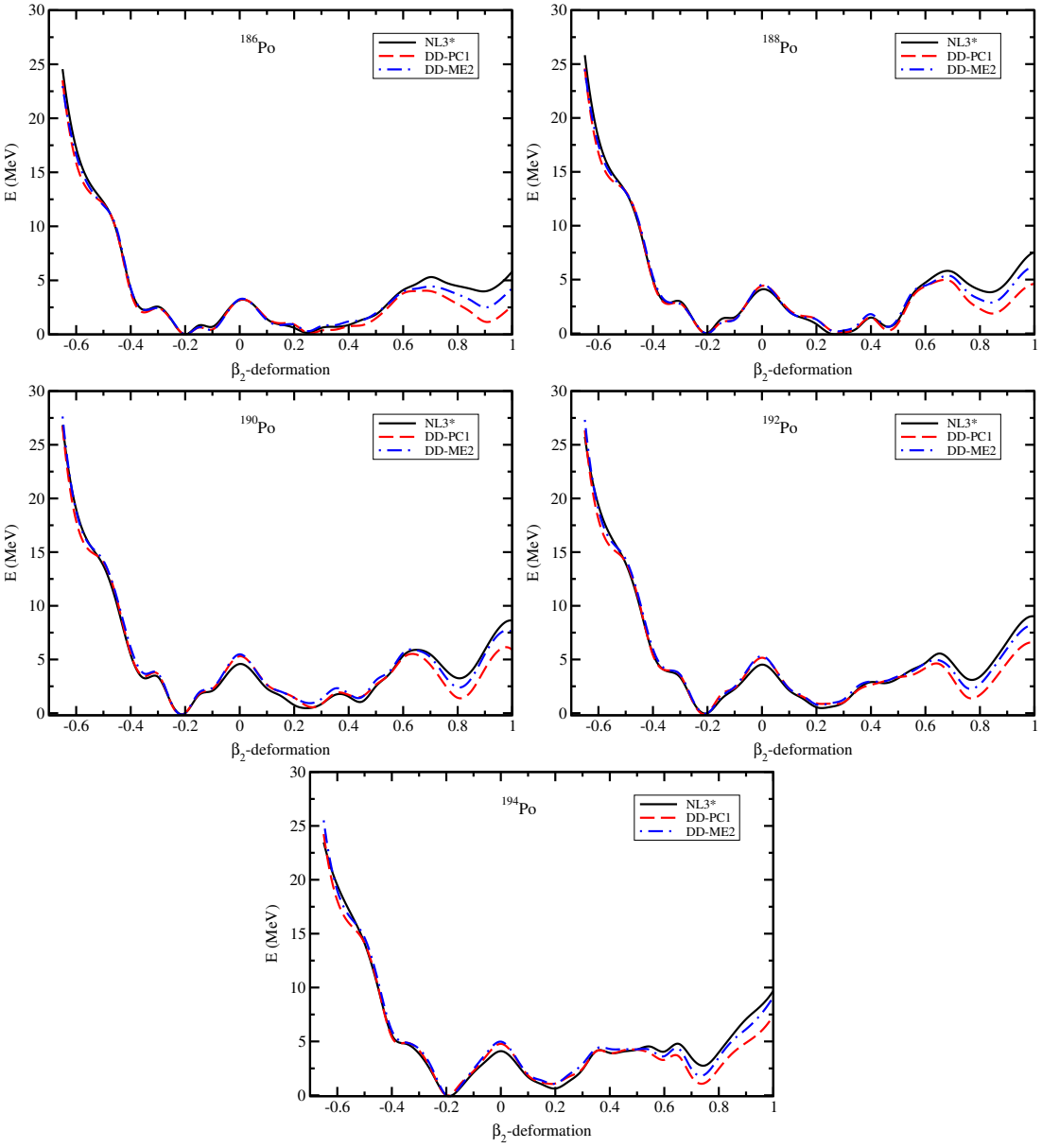

FIGURE 3.18: Potential energy curves for even-even Po isotopes with N ranging from 102 to 110 as functions of the quadrupole deformation β_2. The effective interactions used are NL3*, DD-ME2, and DD-PC1. The curves are scaled such that the ground state has a zero MeV energy

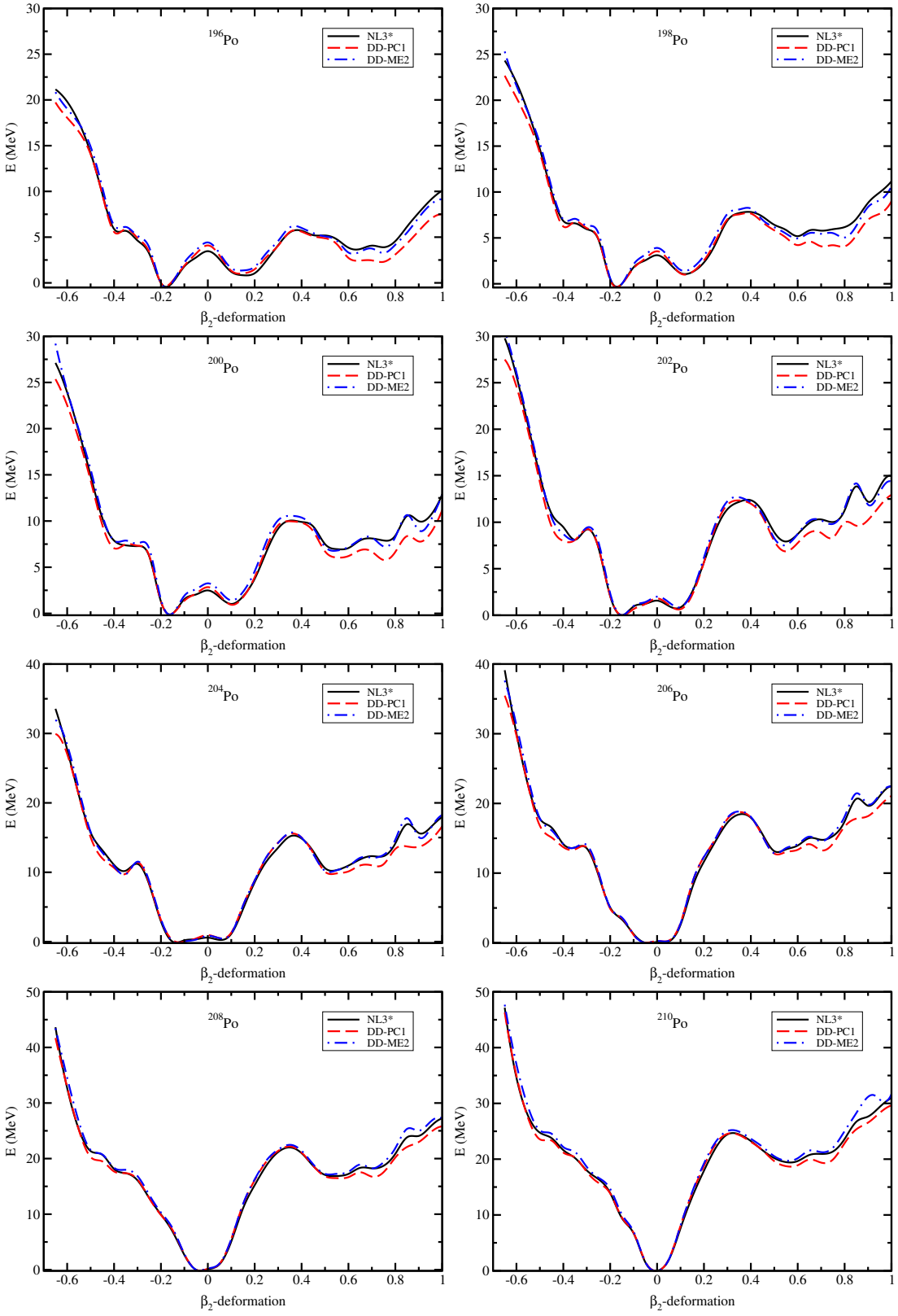
196Po
198Po
200Po
202Po
204Po
206Po
208Po
210Po
NL3*
DD-PC1
DD-ME2
E (MeV)
β2-deformation

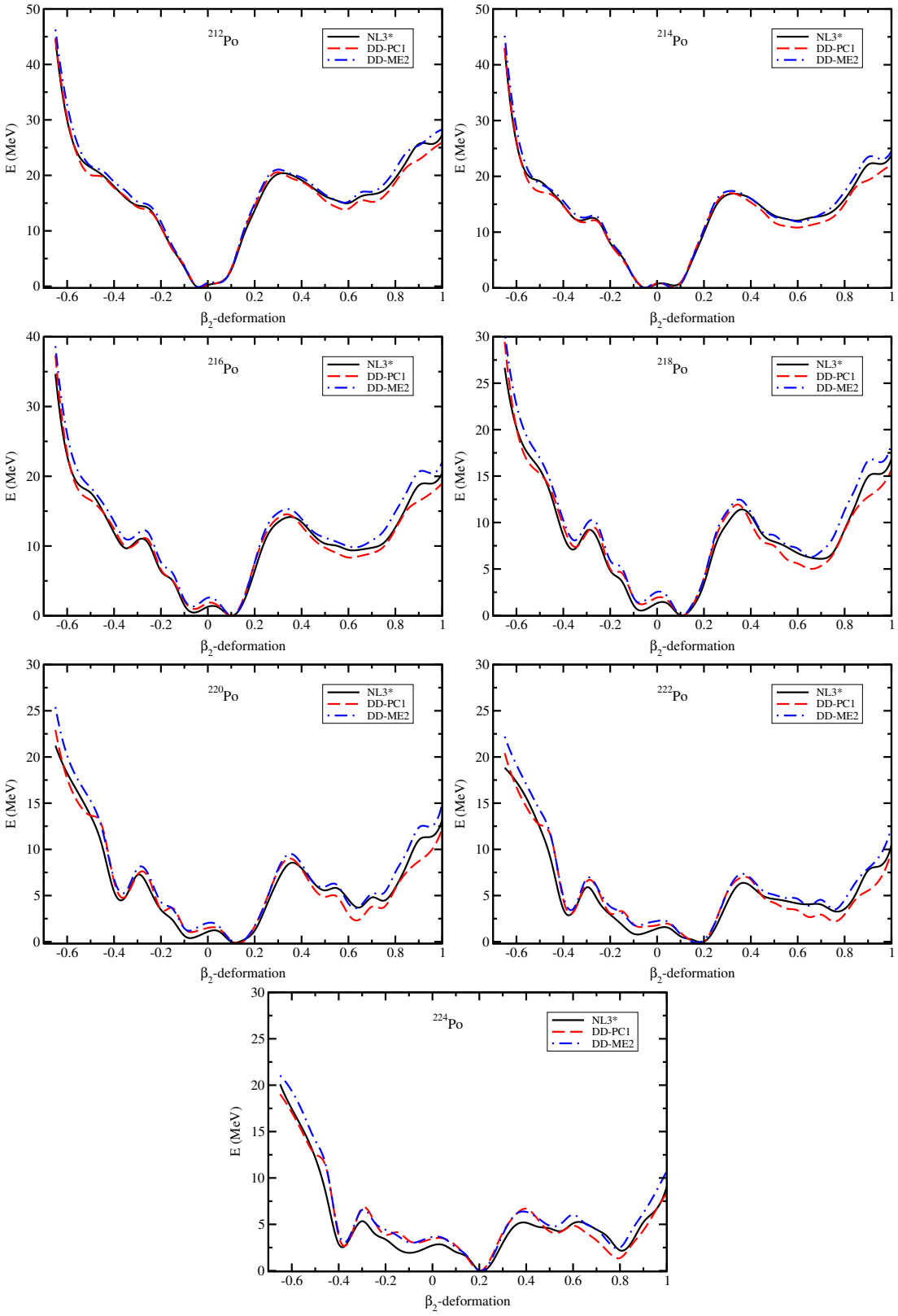

FIGURE 3.19: Same as Fig.3.18, but for $112 \leq N \leq 140$

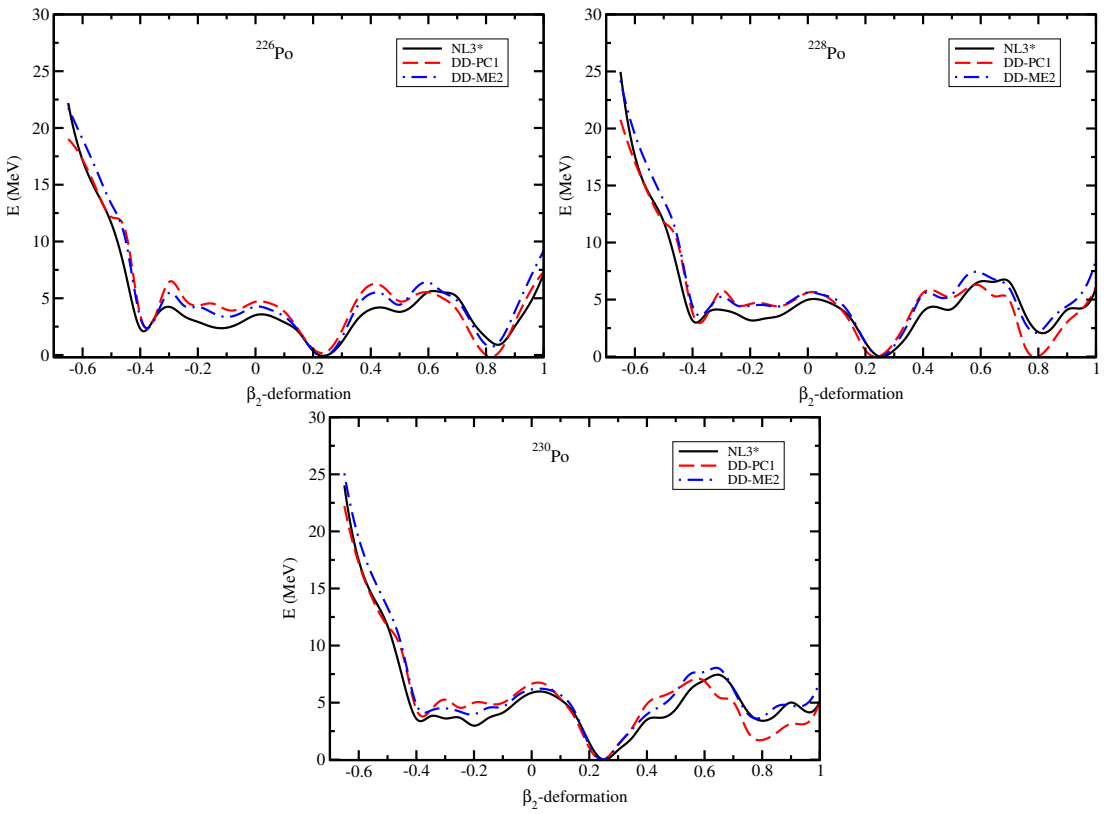

FIGURE 3.20: Same as Fig.3.18, but for $142 \leq N \leq 146$

On the other hand, Fig.3.20, shows that the β_2 value, where the saddle point take a place is no longer smaller, for the heavier isotopes. For ^{226}Po, ^{228}Po and ^{230}Po, β_2 values are 0.6, 0.68 and 0.65 respectively.

The lack of double-humped barrier, in the investigated neutron-rich Po isotopes, is a noteworthy feature. In the sense, all of these nuclei exhibit only a single barrier as observed in Figs.3.18-3.20.

3.3.2 Heights of fission barrier

Of particular importance now is the height of the fission barrier. The CDFT calculation of the barrier heights, of a given Po isotopes, with the deformation β_2, then proceeds as described in the previous sections.

All the nuclei of Table 3.5 exhibit only a single barrier, we show the height of this barrier, in the three parmetrizations, we show also the corresponding deformation parameter β_2. The sensitivity of barrier location to the neutron number N, shown in this table, was discussed in the previous subsection.

Table 3.5: Calculated fission barrier heights in (MeV) for Po nuclei, with forces NL3*, DD-PC1 and DD-ME2 within the CDFT framework. ^{i} and ^{o} refer to inner and outer barriers, respectively.

		NL3*		**DD-PC1**		**DD-ME2**	
N	A	β_2	B_f	β_2	B_f	β_2	B_f
			Z=84 (Po)				
102	186	0.7	5.16	0.65	3.90	0.7	4.14
104	188	0.7	5.00	0.65	4.49	0.7	4.54
106	190	0.65	4.82	0.65	3.88	0.65	4.35
108	192	0.65	5.00	0.65	3.70	0.65	4.00
110	194	0.65	4.16	0.5	3.13	0.65	3.28
112	196	0.4	4.87	0.4	4.56	0.35	4.71
114	198	0.4	6.65	0.4	6.53	0.4	6.69
116	200	0.35	9.02	0.35	9.03	0.35	9.14
118	202	0.4	11.53	0.35	11.70	0.35	11.82
120	204	0.35	14.90	0.35	15.02	0.35	15.19
122	206	0.35	18.32	0.35	18.49	0.35	18.58
124	208	0.35	21.90	0.35	22.05	0.35	22.24
126	210	0.35	24.45	0.3	24.54	0.3	25.04
128	212	0.3	20.02	0.3	20.18	0.3	20.41
130	214	0.35	16.19	0.3	16.61	0.3	17.08
132	216	0.35	14.16	0.35	14.46	0.35	15.27
134	218	0.35	11.34	0.35	11.91	0.35	12.48
136	220	0.35	8.49	0.35	9.00	0.35	9.51
138	222	0.35	6.22	0.35	6.84	0.35	7.25
140	224	0.39	5.28	0.4	6.68	0.4	6.34
142	226	0.6	5.55	0.4	5.85	0.6	6.40
144	228	0.68	6.81	0.6	6.13	0.6	7.35
146	230	0.65	7.44	0.58	7.20	0.65	8.00

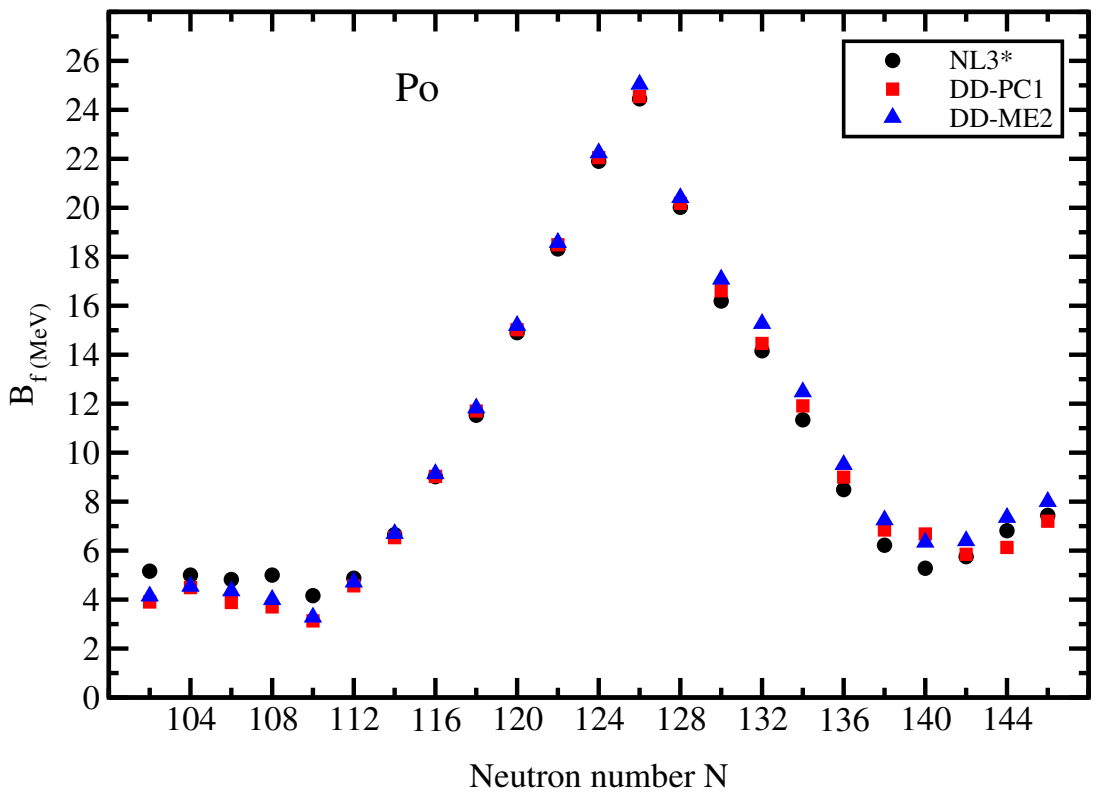

FIGURE 3.21: Fission barrier heights for Po nuclei as a function of neutron number N, Obtained with the NL3*(black circles), DD-PC1(red squares) and DD-ME2(blue triangles) parametrizations of RMF Lagrangian.

The calculated heights of fission barriers, in the three parmetrizations of Table 3.5, are shown in Fig.3.21, as a function of neutron number N, as well as we label in Fig.3.21. A comparison show that the three calculations provide values close to each other. On the contrary, the DD-ME2 parametrization produces barriers, which are (on average) with difference not exceeding 1.3 MeV, higher than the ones obtained in the NL3* and the DD-PC1 parametrization, for most of the nuclei in question. It may be noted that the PEC 3.18-3.20, presented earlier look similar in these parametrizations, and thus, we believe that the heights, and the positions of the fission barriers, are independent of parametrization.

3.3.3 Comparison with experimental data and other theoretical models

The validity of our results, are verified here by making a comparison with experimental data [56], and theoretical prediction from different models. Specifically the FRLDM, the SHF, the ETFSI, and the MM models, described in the preceding sections. Only the FRLDM calculation covers all the Po nuclei in question, while the rest of calculations mentioned above, include a few measured nuclei.

In Table 3.6 and Fig.3.22, we first compare our NL3* results, with those obtained from the FRLDM model. Such comparison, show a good prospective, the two models have the same tendency concerns the behavior of fission barrier heights, throughout the isotopic chain. On the other hand, the FRLDM barriers come slightly higher than ours. Nothing can be guessed, according to the tendency of barrier heights, based on ETFSI, SHF and MM calculations, as we have already pointed out in the subsections 3.1.3 and 3.2.3 . We can only note that, the MM barriers are higher than ours, for the subsequent $140 \leq N \leq 146$. While both FRLDM and SHF models significantly underestimate the barrier, for the nuclei with $N = 124$ up to $N = 128$, shown in the same figure.

Table 3.6: Comparison of fission barrier heights from NL3*parametrizations, with other theoretical evaluations: SHF [21], FRLDM [23], ETFSI [17, 18], CDFT (present work), and experimental data taken from Ref.[56]. All quantities are in (MeV), except for numbers specifying the nucleus. Dashes mean not measured or not calculated.

Z	N	A	CDFT	FRLDM	ETFSI	SHF	MM	EXP
84	102	186	5.16	6.35	-	-	-	-
	104	188	5.00	6.92	-	-	-	-
	106	190	4.82	7.55	-	-	-	-
	108	192	5.00	8.25	-	-	-	-
	110	194	4.16	9.46	-	-	-	-
	112	196	4.87	10.29	-	-	-	-
	114	198	6.65	11.52	-	-	-	-
	116	200	9.02	13.31	-	-	-	-
	118	202	11.53	15.41	-	-	-	-
	120	204	14.90	17.02	-	-	-	-
	122	206	18.32	19.02	-	-	-	-
	124	208	21.90	20.81	15.1	13.9	-	19.9
	126	210	24.45	22.14	17.1	14.8	-	21.2
	128	212	20.02	20.27	14.9	13.8	-	19.6
	130	214	16.19	17.76	-	-	-	-
	132	216	14.16	15.42	-	-	-	-
	134	218	11.34	13.85	-	-	-	-
	136	220	8.49	12.47	-	-	-	-
	138	222	6.22	11.91	-	-	-	-
	140	224	6.68*	11.46	-	-	13.81	-
	142	226	5.55	10.98	-	-	12.23	-
	144	228	6.81	10.68	-	-	11.53	-
	146	230	7.44	10.63	-	-	10.99	-

* From DD-PC1 Parametrization.

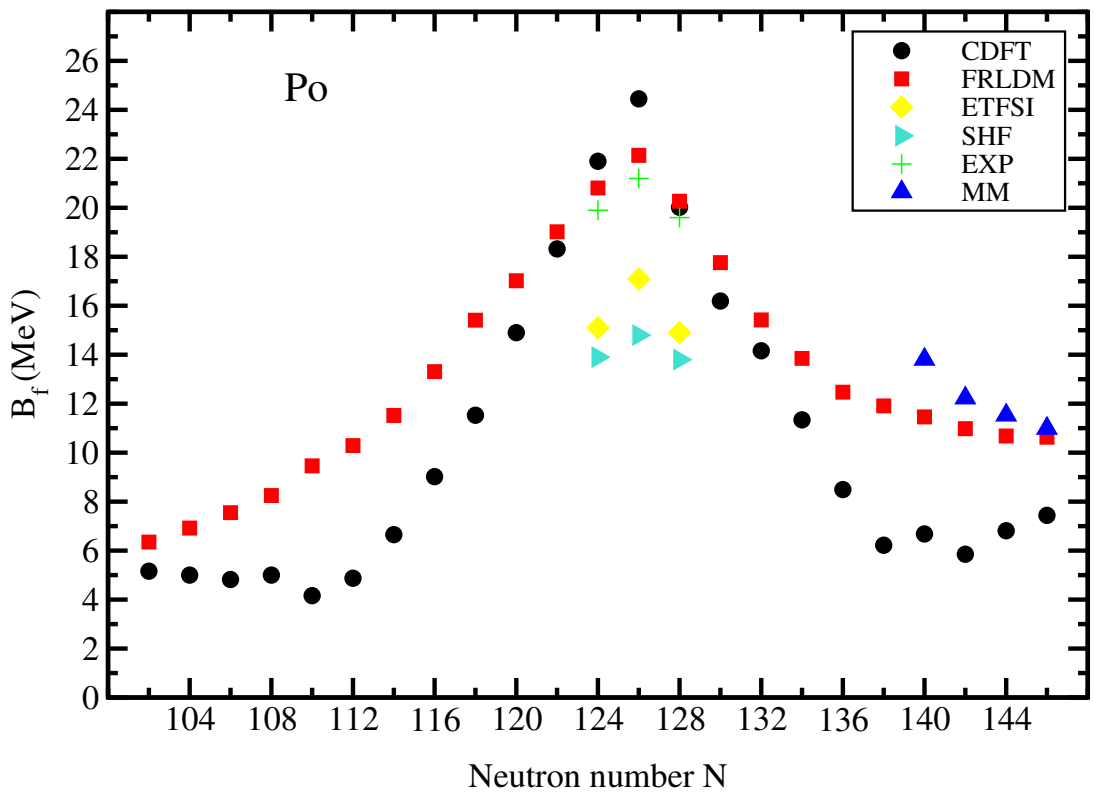

FIGURE 3.22: Comparison of fission barriers as a function of neutron number N, calculated by Moller et al.(FRLDM)(Ref.[23]), Mamdouh et al.(ETFSI)(Ref.[17, 18]), Samyn et al.(SHF)(Ref.[21]), Howard et al.(MM)(Ref.[4]) and by us (CDFT), with experimental data (EXP)(Ref.[56]).

It is gratifying to see now, for this group of nuclei, the level of agreement of our model with experiment. Unfortunately, an experimental value is available for ^{208}Po, ^{210}Po and ^{212}Po nuclei only. For these, we show in Fig.3.23, the deviation ΔB_f, of our calculated barrier heights from the experimental values; in the same figure, we show also the corresponding quantities, for the FRLDM, the ETFSI and the SHF models.

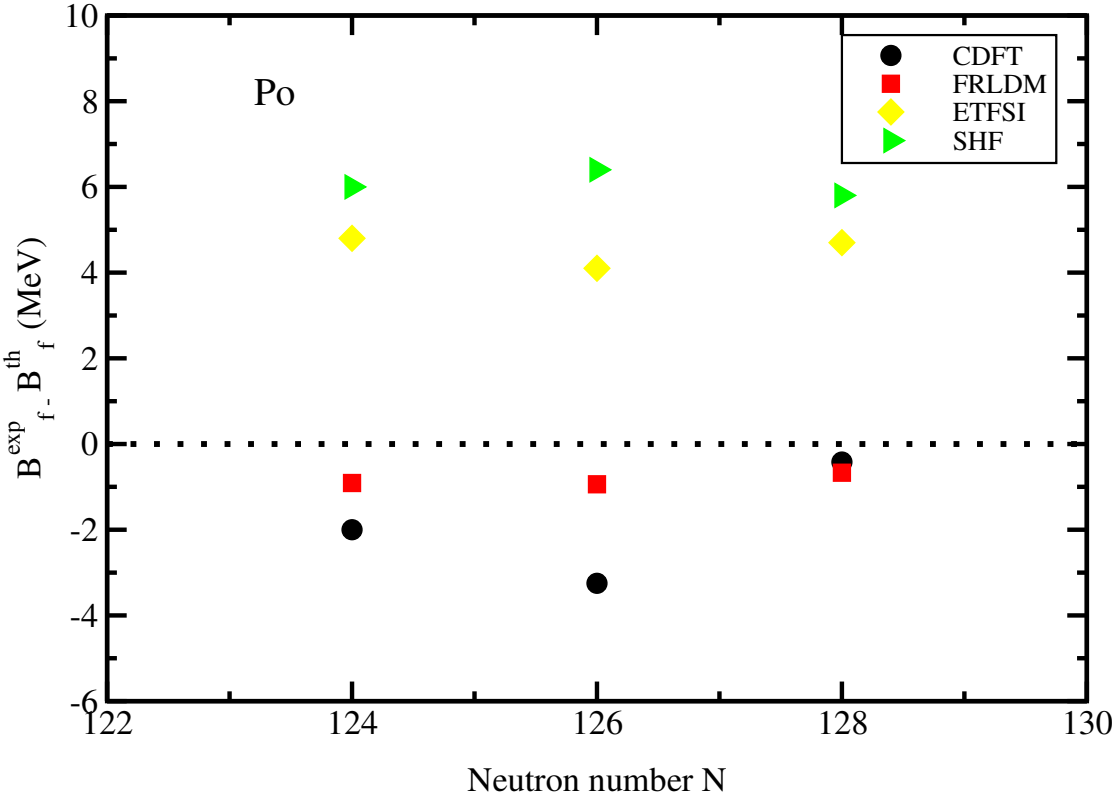

FIGURE 3.23: The difference between experimental and calculated heights of inner fission barriers as a function of neutron number N. The results of the calculations within microscopic-macroscopic method ('SHF(Samyn)' [21]), the finite range liquid-drop model ('FRLDM(Moller)' [23]), the covariant density functional theory ('CDFT') and the extended Thomas-Fermi plus Strutinsky integral ('ETFSI(Mamdouh)' [17, 18]) are shown.

Our calculated values come higher than the experimental values, with deviation about 2 MeV, for the nucleus with $N = 124$, and 3 MeV in the case of $N = 126$ nucleus. Our calculated value, was better for $N = 128$ nucleus, with deviation around 0.4 MeV from the experimental value. The FRLDM predict the barriers to be < 1 MeV higher than the experimental ones, for these nuclei, but the agreement is, however, much better. On the other hand, calculations based on the ETFSI and the SHF, predict the barriers to be 4-5 MeV, about 6 MeV, lower than the experimental ones, respectively.

3.4 Radon ($_{86}$Rn) isotopes

3.4.1 Potential energy curves

We now extend toward highly neutron rich even-even Rn nuclei ($104 \leq N \leq 146$). The potential energy curves "PEC" have been constructed. For each nucleus, potential energy plotted versus the deformation β_2, in Figs.3.24-3.26. We discuss these figures only briefly here, since similar results have been obtained in our calculations for Hg sec.3.1, Pb sec.3.2 and Po sec.3.3 nuclei.

The lighter nuclei, beginning with $A = 190$ up to $A = 232$, exhibit a single barrier at very high deformation, The β_2 values are hung around 0.65 as observed in Fig.3.24. This is come similar to the result we already predicted, for the lighter nuclei in the Po region. Probably, this is the most striking feature of the CDFT barrier calculations, of highly neutron rich nuclei.

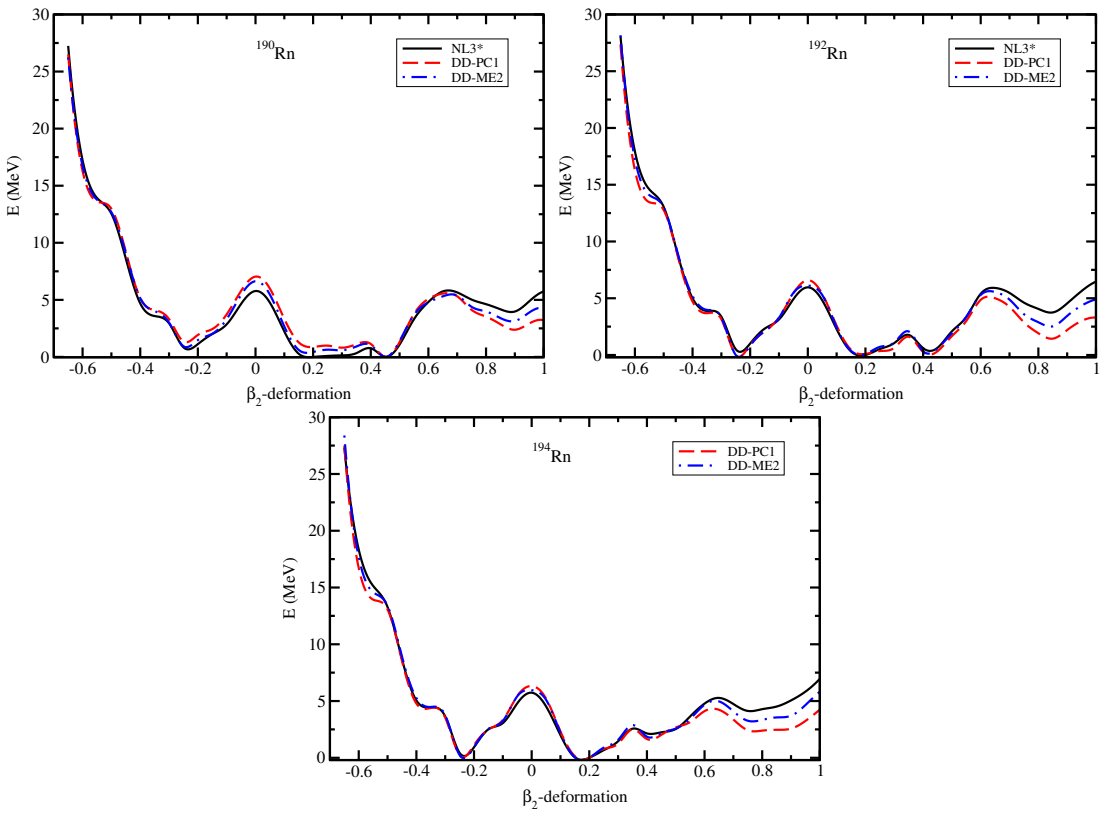

FIGURE 3.24: Potential energy curves for even-even Rn isotopes with N ranging from 104 to 106 as functions of the quadrupole deformation β_2. The effective interactions used are NL3*, DD-ME2, and DD-PC1. The curves are scaled such that the ground state has a zero MeV energy

In Fig.3.25, PEC of Rn nuclei with N ranging from 110 to 140 are presented. With a further increase in the neutron number N, i.e., on going from lighter isotopes Fig.3.24, to the heavier ones, the PEC curve maximum take place at lower deformations. For this subset of the investigated nuclei, our calculations predict the β_2 values, to swing between 0.3, 0.35 and 0.4. This tendency is also visible in Table 3.7.

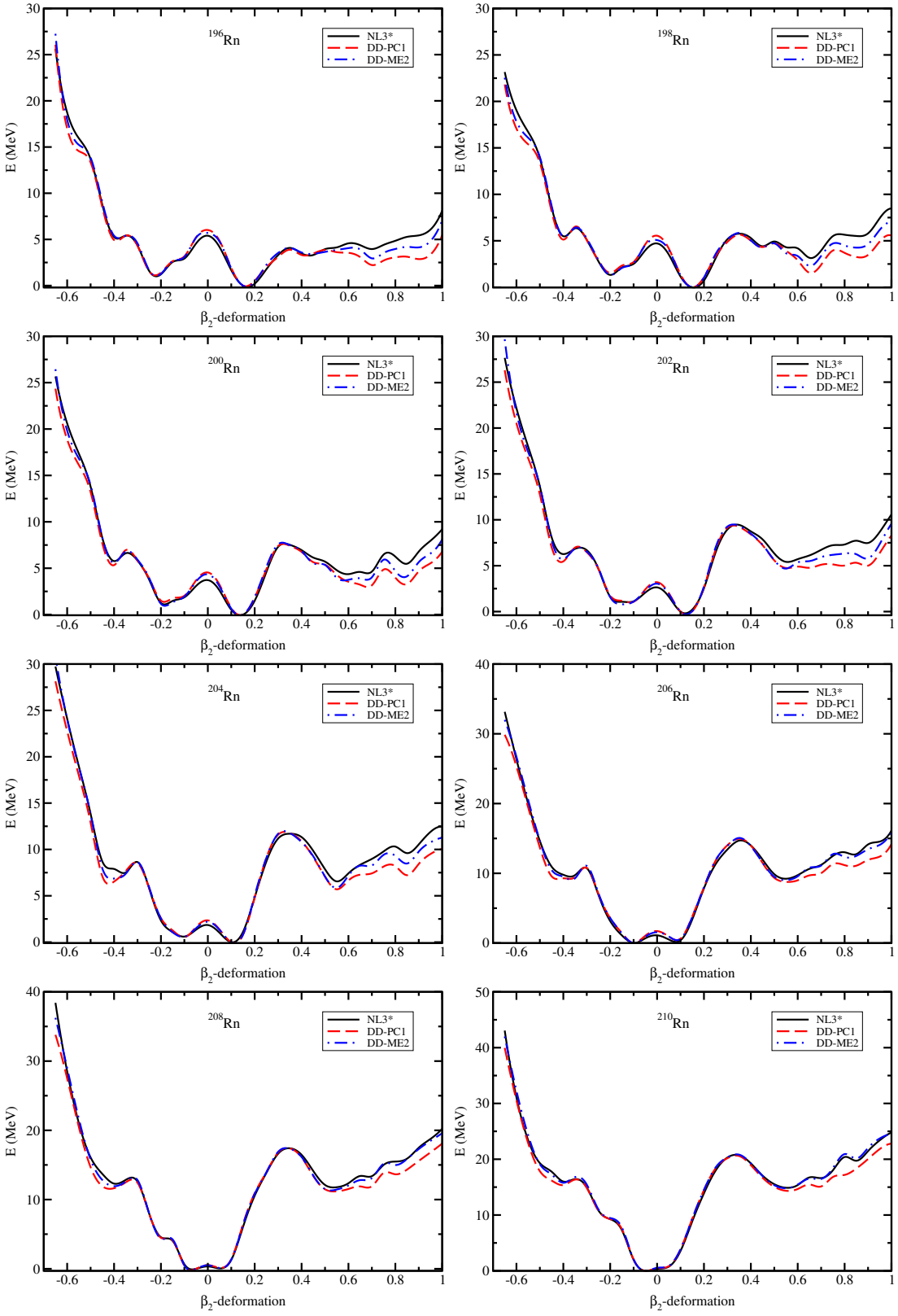
196Rn
198Rn
200Rn
202Rn
204Rn
206Rn
208Rn
210Rn
NL3*
DD-PC1
DD-ME2
E (MeV)
β2-deformation

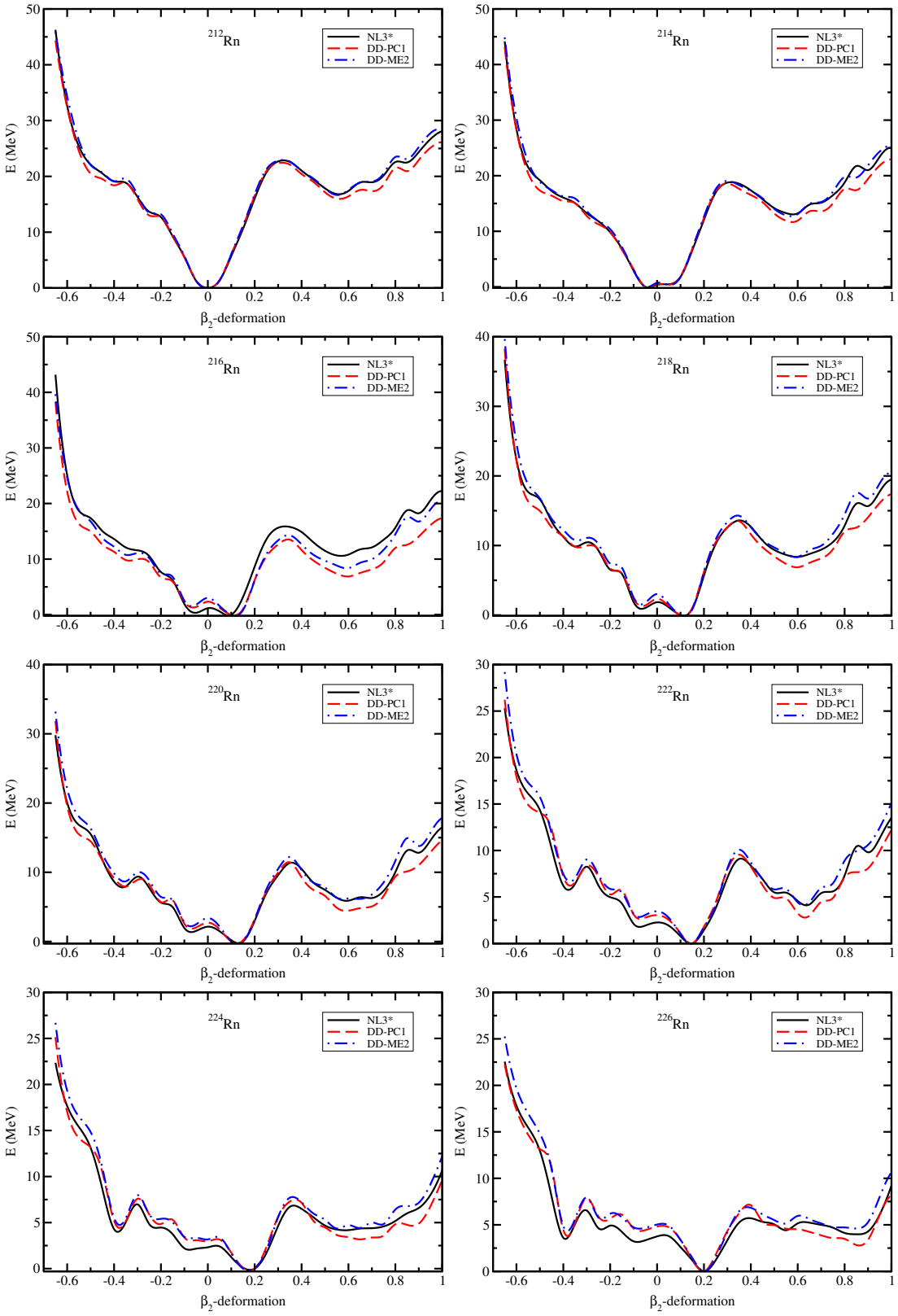

FIGURE 3.25: Same as Fig.3.24, but for $110 \leq N \leq 140$

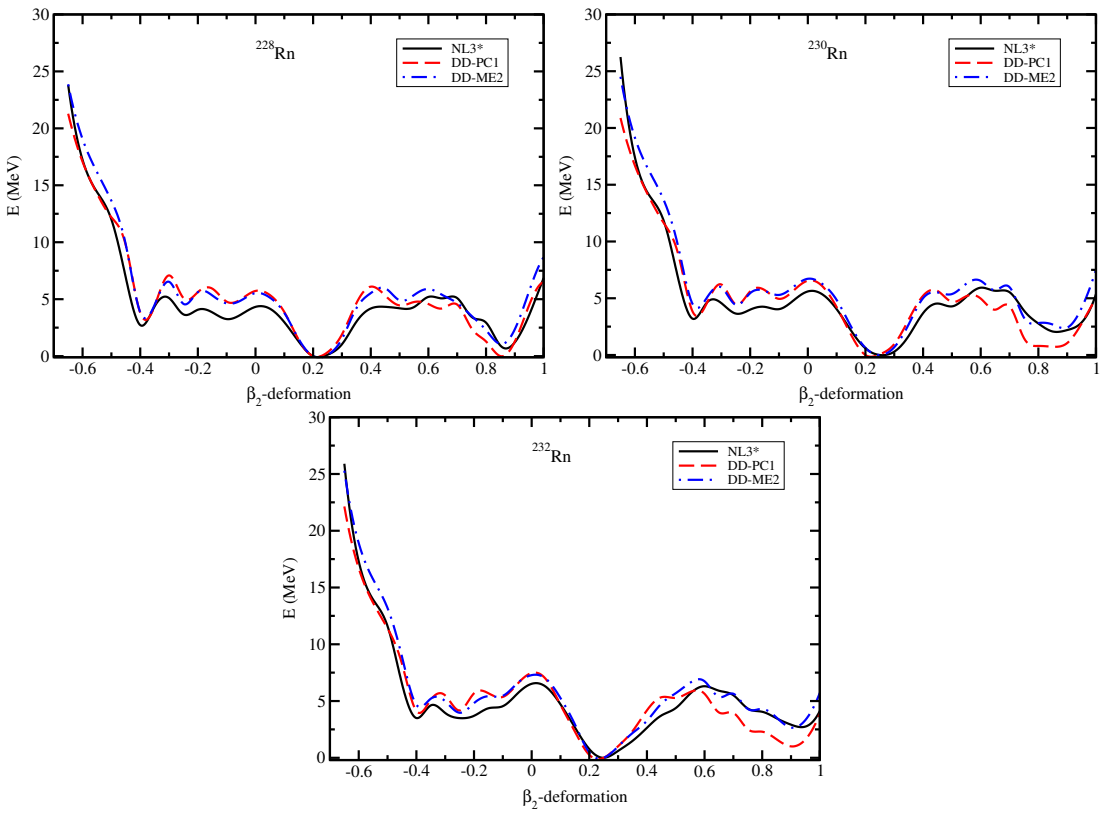

FIGURE 3.26: Same as Fig.3.24, but for $142 \leq N \leq 146$

It is to be remarked here, that Fig.3.26 revive the old trend of the isotopic variation, observed in Hg, Pb and Po nuclei. That is the β_2 value, where the saddle point arise, for the heavier Rn isotopes, ^{228}Rn, ^{230}Rn and ^{232}Rn, is not lower than that of the lighter ones, but higher. These nuclei exhibit the barrier hang around 0.6.

Such behavior is a generic, noteworthy Feature of deformed nuclei include almost all isotopic chains in the investigated region.

3.4.2 Heights of fission barrier

Our interest lies mainly with barrier heights B_f. We now extract barrier heights B_f, in the three parametrizations, for Rn isotopes. These results are presented in Table 3.7 and in Fig.3.27. In Table 3.7, we show also the corresponding deformation parameter β_2 value for each calculated barrier.

The calculated heights of fission barriers, in the three parmetrizations, of Table 3.7, are plotted as a function of neutron number N, in Fig.3.21. The three calculations provide values very close to each other. The barriers are (on average) with difference never exceeds 1.6 MeV, for all of the nuclei in question.

TABLE 3.7: Calculated fission barrier heights in (MeV) for Rn nuclei, with forces NL3*, DD-PC1 and DD-ME2 within the CDFT framework. ^{i} and ^{o} refer to inner and outer barriers, respectively.

		NL3*		**DD-PC1**		**DD-ME2**	
N	A	β_2	B_f	β_2	B_f	β_2	B_f
			Z=86 (Rn)				
104	190	0.65	5.72	0.65	5.55	0.7	5.38
106	192	0.65	5.30	0.65	4.73	0.65	5.21
108	194	0.65	5.27	0.65	4.23	0.65	4.97
110	196	0.35	4.08	0.35	3.88	0.6	4.06
112	198	0.35	5.77	0.35	5.66	0.35	5.84
114	200	0.35	7.52	0.35	7.41	0.3	7.58
116	202	0.35	9.44	0.35	9.23	0.35	9.33
118	204	0.35	11.69	0.35	11.77	0.35	11.77
120	206	0.35	14.29	0.35	14.31	0.35	14.47
122	208	0.35	17.35	0.35	17.24	0.35	17.22
124	210	0.35	20.34	0.35	20.13	0.35	20.28
126	212	0.3	22.69	0.3	22.38	0.3	22.80
128	214	0.3	18.40	0.3	18.20	0.3	18.70
130	216	0.35	15.78	0.3	15.54	0.3	16.29
132	218	0.35	13.60	0.35	13.50	0.35	14.28
134	220	0.35	11.34	0.35	11.45	0.35	12.20
136	222	0.35	9.08	0.35	9.54	0.35	10.07
138	224	0.35	6.71	0.37	7.53	0.37	7.90
140	226	0.4	5.71	0.39	7.27	0.39	6.96
142	228	0.61	5.31	0.4	6.10	0.45	6.15
144	230	0.6	5.93	0.45	5.65	0.59	6.76
146	232	0.6	6.30	0.58	5.91	0.58	7.02

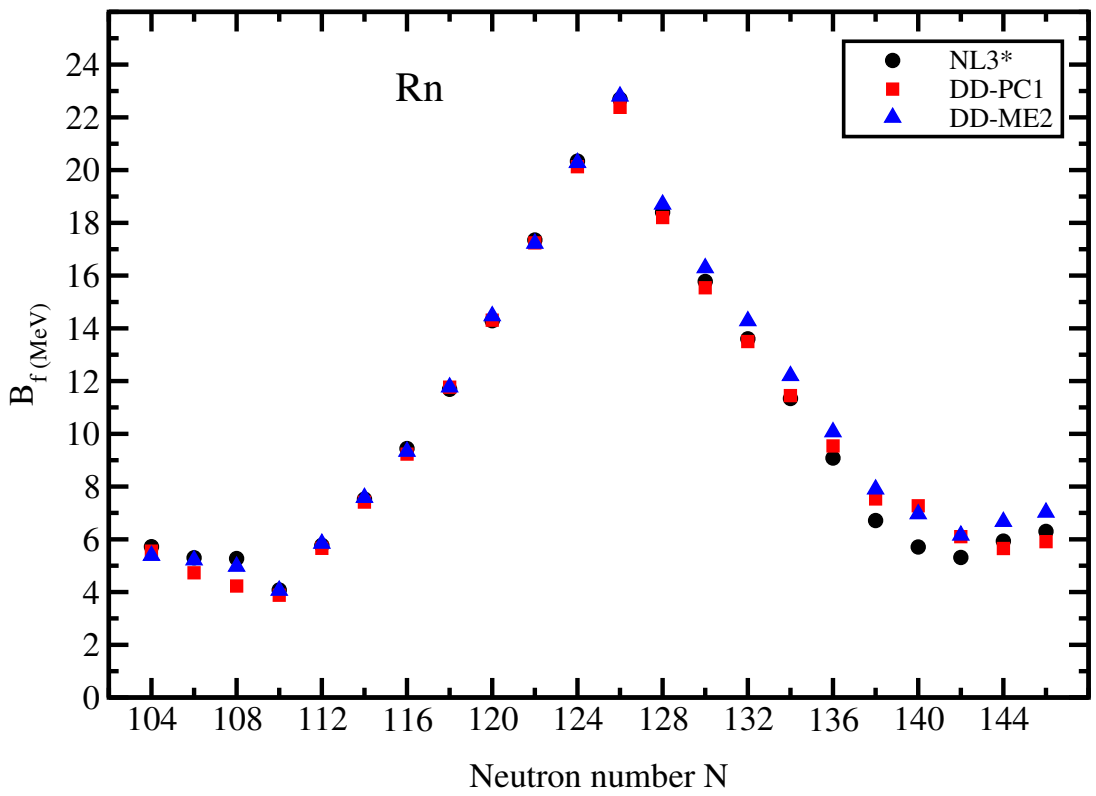

FIGURE 3.27: Fission barrier heights for Rn nuclei as a function of neutron number N, Obtained with the NL3*(black circles), DD-PC1(red squares) and DD-ME2(blue triangles) parametrizations of RMF Lagrangian.

The PEC 3.24-3.26, presented earlier tend to be the same in these parmetrizations, therefore, we can say that the heights and the positions of the fission barriers, are independent of parametrization.

3.4.3 Comparison with experimental data and other theoretical models

In this subsection, the comparison with data will be made just with the NL3* results. Because no fission experimental data are available for Rn (Z=86) nuclei,

we are unable to assess the deviation of our calculated barriers, in the investigated region. We therefore compare with the available theoretical calculations, namely, the FRLDM, the SHF, the ETFSI, and the MM models as in all the previous work. These results for fission barrier heights, where available, are presented in Table 3.8, in relation with our predictions for the same barriers.

We display these comparisons, in Table 3.8 and in Fig.3.28. The comparison of our results, with those obtained from the FRLDM and MM models, shows that the latter predictions for the few nuclei, where available, are systematically higher than ours. The trends of our barriers agree well with the FRLDM ones, the discrepancy is $\sim$ 0-4 MeV, with either sign being possible.

Table 3.8: Comparison of fission barrier heights with other theoretical evaluations: SHF [21], FRLDM [23], ETFSI [17, 18], CDFT (present work), and experimental data taken from Ref.[56]. All barriers are from NL3* parametrizations, except as indicated in footnote. All quantities are in (MeV), except for numbers specifying the nucleus. Dashes mean not measured or not calculated.

Z	N	A	CDFT	FRLDM	ETFSI	SHF	MM	EXP
86	104	190	5.72	4.54	-	-	-	-
	106	192	5.30	4.63	-	-	-	-
	108	194	5.27	5.43	-	-	-	-
	110	196	4.08	6.41	-	-	-	-
	112	198	5.77	7.40	-	-	-	-
	114	200	7.52	8.61	-	-	-	-
	116	202	9.44	10.29	-	-	-	-
	118	204	11.69	12.10	-	-	-	-
	120	206	14.29	14.20	-	-	-	-
	122	208	17.35	15.94	-	-	-	-
	124	210	20.34	17.61	-	-	-	-
	126	212	22.69	18.63	-	-	-	-
	128	214	18.40	16.69	-	-	-	-
	130	216	15.78	14.24	10.1	9.8	-	13.5
	132	218	13.60	12.83	-	-	-	-
	134	220	11.34	11.47	-	-	-	-
	136	222	9.08	10.82	-	-	-	-
	138	224	6.71	10.30	-	-	-	-
	140	226	5.71	9.45	-	-	11.10	-
	142	228	6.10	9.04	-	-	10.46	-
	144	230	5.65*	8.81	-	-	9.82	-
	146	232	6.30	8.82	-	-	9.34	-

* From DD-PC1 Parametrization.

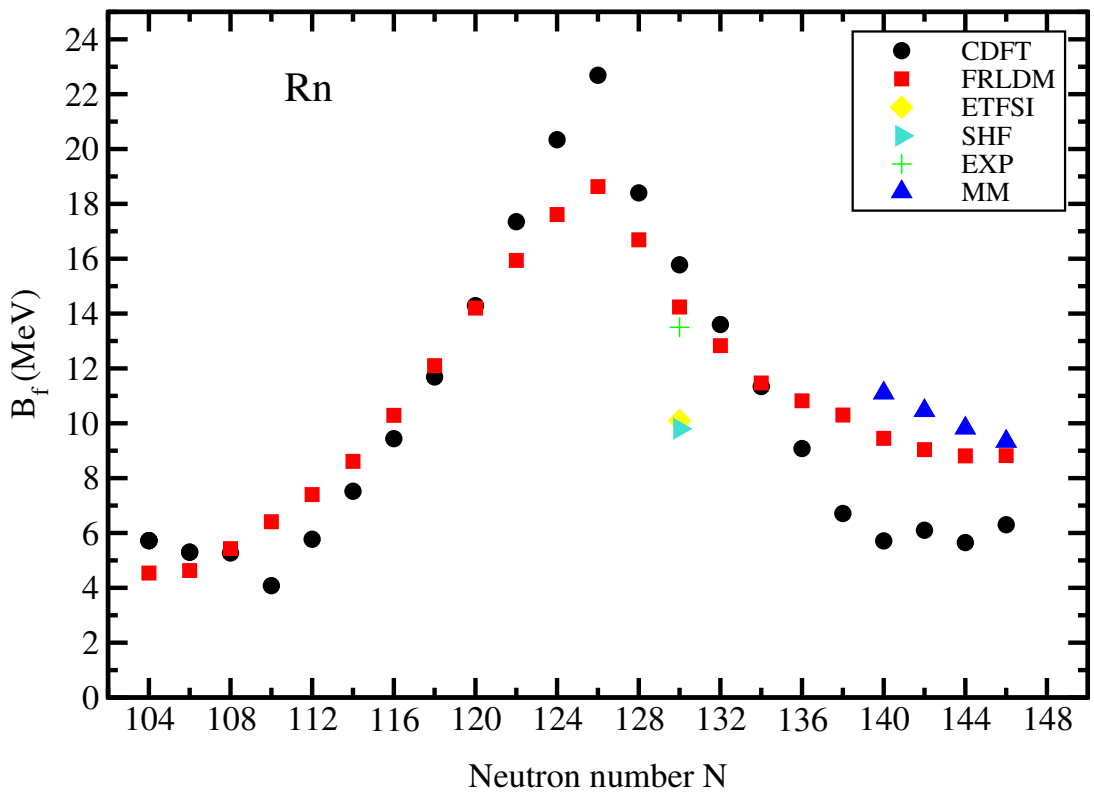

FIGURE 3.28: Comparison of fission barriers as a function of neutron number N, calculated by Moller et al.(FRLDM)(Ref.[23]), Mamdouh et al.(ETFSI)(Ref.[17, 18]), Samyn et al.(SHF)(Ref.[21]), Howard et al.(MM)(Ref.[4]) and by us (CDFT) with experimental data (EXP)(Ref.[56]).

Our result for the Rn isotope ($N = 130$), lie higher than the values obtained using the other model, it is higher than the experimental one too. The discrepancy with respect to experiment is $\sim$ 2.3 MeV. A lager agreement with the experiment, is observed for the FRLDM calculated value, which is 0.74 MeV higher than the experimental one. The obtained ETFSI and SHF barrier is underestimated by about 4 MeV, as it is obvious in Fig.3.28.

Chapter 4

Conclusion

The following conclusion can be drawn from our calculation, within covariant density functional theory, that was devoted to the fission barrier height B_f, in the pre-actinide region $80 \leq Z \leq 86$. Three different classes of models with parameterizations NL3*, DD-PC1 and DD-ME2 were used in the calculations.

- The above presented model has been successfully applied to more than 20 even-even selected isotopes, for Hg, Pb, Po, and Rn nuclei, for which data exist. Only for Hg ($98 \leq N \leq 102$) and Pb ($N = 178, 180$), more than one saddle point has been observed (for these nuclei, we consider only the highest one). On contrary, Po and Rn nuclei did not exhibit this feature.

- The question arise, as to whether the double barriers that we found out are real or not. There is certainly, no experimental confirmation for the double-humped barriers that we predicted.

- The tendency for saddle point emergence to a lower deformation, has been observed, as a result of neutron number increasing. It should be noted that, for a given value of Z there is, of course some isotopic variation, in particular for the heavier isotopes in each isotopic chain, in which, we found out the barrier take place at higher deformation again.

- For each nucleus, fission barrier heights were presented, as well as their deformation parameter β_2, obtained in the three parametrizations. Fission barriers heights and positions tend to be very similar in the three parametrizations. The DD-ME2 parametrization produces barriers which are(on average) with difference not exceeding 1.6 MeV, higher than the ones obtained in the NL3* and the DD-PC1 parametrization, for all of the nuclei in question.

- In Fig.4.1, we display the height of the fission barrier B_f, for these nuclei, as the difference between the highest saddle-point and the ground-state energy. The barrier heights were as follows; in the range of 4.33-23.45 , 3.68-26.44, 4.16-24.45 and 4.08-22.69 MeV, for Hg, Pb, Po and Rn isotopes, respectively.

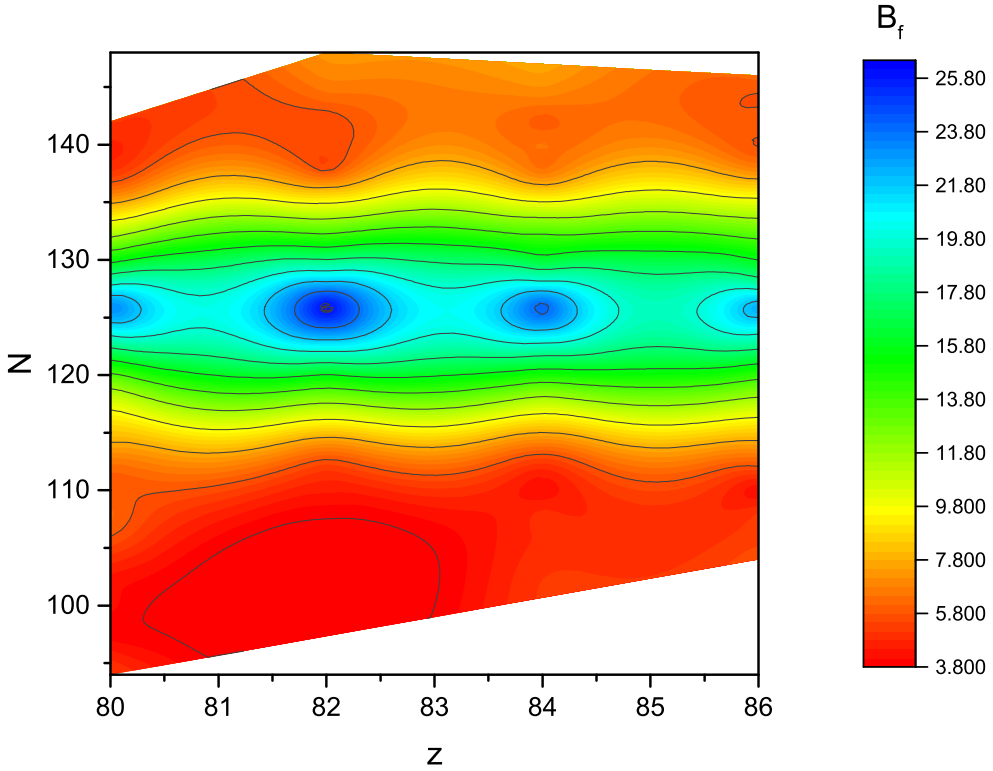

FIGURE 4.1: Contour map of calculated fission barrier heights B_f for even-even pre-actinide nuclei in the range of proton number $82 \leq Z \leq 86$ and neutron number $94 \leq N \leq 148$.

- We found out that, for given value of Z, the barrier tend to increase with N, the calculated heights show a maximum at $N = 126$, and then with increasing N fall to a minimum at around $N = 140$. While the height of the barrier remains remarkably constant as Z increase, for a given value of N.

- No comparison with experiment is yet possible, for most of the calculated fission barriers in the pre-actinide region. Fig.4.2 show the differences between experimental and calculated heights of fission barriers, obtained in different theoretical models as a function of neutron number N.

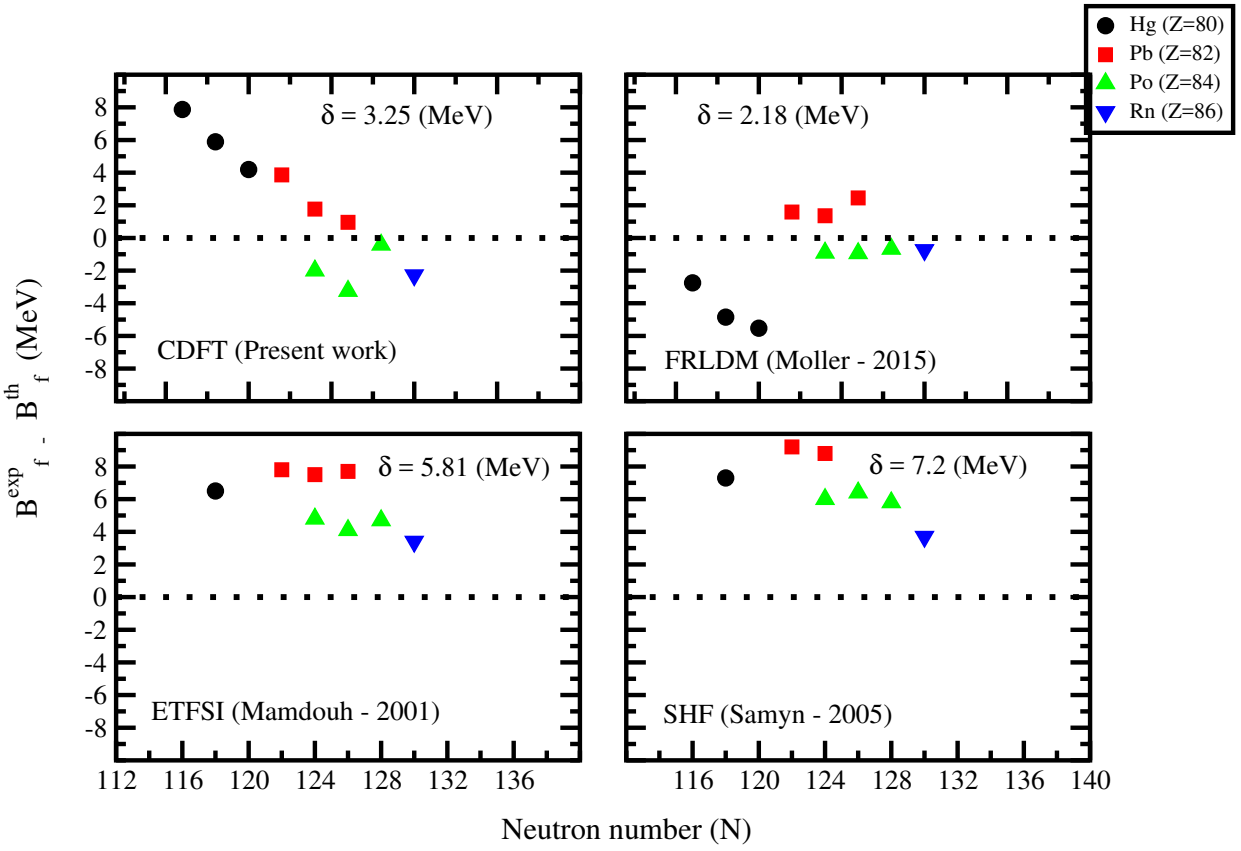

FIGURE 4.2: The difference between experimental and calculated heights of fission barriers, as a function of neutron number N. The results of the calculations within CDFT, FRLDM, ETFSI and SHF are shown. Note that this comparison covers only results with known experimental barriers.

- The average deviation per barrier δ [in MeV] displayed in Fig.4.2, is defined as $\delta = \sum_{i=1}^{N} \mid B_f^i(\text{th}) - B_f^i(\text{exp}) \mid /N$, where N is the number of the barriers with known experimental heights, and $B_f(\text{th})$, $B_f(\text{exp})$ are calculated, experimental heights of the barriers.

- One can see from Fig.4.2, that The largest discrepancy of our calculation with the experimental data, is about 8 MeV, obtained for Hg isotopes. The agreement is better for Pb, Po and Rn isotopes in this restricted region.

- The agreement with experiment is the best for the FRLDM calculation, with deviation of 2.18 MeV. Nevertheless, our calculation is reasonable comparing with the ETFSI and the SHF ones.

- Theoretical evaluations of fission barrier heights based on various models, differ between each other significantly. Important differences can, however, be observed in the shape parametrization of a fissioning nucleus, and thus in the deformation space used in the calculation.

Bibliography

[1] P. Möller and J. R. Nix, in Proceedings, Third IAEA Symposium on Physics and Chemistry of Fission, Rochester, 1973 (IAEA, Vienna, 1974), Vol. 1, p. 103.

[2] W. M. Howard and J. R. Nix, in Proceedings, Third IAEA Symposium on Physics and Chemistry of Fission, Rochester, 1973 (IAEA Vienna, 1974), Vol. 1, p. 145.

[3] P. Möller and J. R. Nix, At. Data Nucl. Data Tables 26, 165 (1981).

[4] W. Howard and P. Möller, At. Data Nucl. Data Tables 25, 219 (1980).

[5] S. E. Larsson and G. Leander, in Proceedings, Third IAEA Symposium on Physics and Chemistry of Fission, Rochester, 1973 (IAEA Vienna, 1974), Vol. 1, p. 172.

[6] H. Ströher, J. Drexler, R. Heil, K. Huber, U. Kneissl, G.Mank, R.Ratzek, H.Ries, T.Weber, W.Wilke, Nucl. Phys. A, (1984).

[7] P. Möller, J. R. Nix, W. D. Myers, and W. J. Swiatecki, At. Data Nucl. Data Tables 59, 185 (1995).

[8] P. Möller, J. R. Nix, and K. L. Kratz, At. Data Nucl. Data Tables 66, 131 (1997).

[9] P. Möller and A. Iwamoto, Acta Phys. Hung. New Ser.: Heavy Ion Phys. 10, 241 (1999).

[10] P. M*exto*ller and A. Iwamoto, Phys. Rev. C. 61, 047602 (2000).

[11] P. Möller, A. J. Sierk, and A. Iwamoto, Phys. Rev. Lett. 92, 072501 (2004).

[12] P. Möller, A. J. Sierk, T. Ichikawa, A. Iwamoto, R. Bengtsson, H. Uhrenholt, and S. berg, Phys. Rev. C. 79, 064304 (2009).

[13] J. Randrup and P. Möller, Phys. Lett. 106, 132503 (2011).

[14] J. Randrup, P. Möller, and A. J. Sierk, Phys. Rev. C. 84, 034613 (2011).

[15] J. L. Egido, L. M. Robledo, and R. R. Chasman, Phys. Lett. B. 393, 13 (1997).

[16] J. F. Berger, M. Girod, and D. Gogny, Nucl. Phys. A. 502, 85 (1989).

[17] A. Mamdouh, J. M. Pearson, M. Rayet, and F. Tondeur, Nucl. Phys. A. 644, 389 (1998).

[18] A. Mamdouh, J. M. Pearson, M. Rayet, and F. Tondeur, Nucl. Phys. A. 679, 337 (2001).

[19] L. Bonneau, P. Quentin, and D. Samsoen, Eur. Phys. J. A. 21, 391 (2004).

[20] T. Bürvenich, M. Bender, J. Maruhn, and P. G. Reinhard, Phys. Rev. C. 69, 029901(E) (2004).

[21] M. Samyn and S. Goriely, Phys. Rev. C. 72, 044316 (2005).

[22] M. Kowal, P. Jachimowicz, and A. Sobiczewski, Phys. Rev. C. 82, 014303 (2010).

[23] P. Möller, A. J. Sierk, T. Ichikawa, A. Iwamoto, and M. Mumpower, Phys. Rev. C. 91, 024310 (2015).

[24] A. Baran, A. Staszczak, M. Warda, M. Kowal, P. G. Reinhard, L. M. Robledo, Nucl. Phys. A. 944 , 0375-9474 (2015).

[25] H. Abusara, A. V. Afanasjev, and P. Ring, Phys. Rev. C. 82, 044303 (2010).

[26] H. Abusara, A. V. Afanasjev, P. Ring, Phys. Rev. C. 85 (2), 024314 (2012).

[27] Z. P. Li, T. Niksic, D. Vretenar, P. Ring, and J. Meng, Phys. Rev. C. 81, 064321 (2010).

[28] P. Ring, H. Abusara, A. V. Afanasjev, G. A. Lalazissis, T. Niksic, and D. Vretenar, Int. J. Mod. Phys. E. 20, 235 (2011).

[29] A. Staszczak, A. Baran, J. Dobaczewski, and W. Nazarewicz, Phys. Rev. C. 80, 014309 (2009).

[30] R. Rodriguez-Guzman, P. Sarriguren, L. M. Robledo, and J. E. Garcia-Ramos, Phys. Rev. C. 81, 024310 (2010).

[31] B. D. Serot, J. D. Walecka, Adv. Nucl. Phys. 16 (1986).

[32] R. J. Furnstahl, B. D. Serot, Comments Nucl. Part. Phys. A. 2, 23 (2000).

[33] T. Mizutani, F. Myhrer, Phys. Rev. D. 35, 1080 (1987).

[34] Y. K. Gambhir, P. Ring, and A. Thimet, ANYALS OF PHYSICS 198, 132-179 (1990).

[35] Y. K. Gambhir, and P. Ring, Modern Phys. Lett. A. 9, 787-795 (1993).

[36] C. M. Shakin, Wei-Dong Sun, and J. Szweda, Phys. Rev. C. 52, 3502 (1995).

[37] P. Ring, J. Phys.: Conf. Ser. 49, 93 (2006).

[38] P. Ring, Prog. Part. Nucl. Phys. 37, 193 (1996) .

[39] J. Boguta and A. R. Bodmer, Nucl. Phys. A. 292, 413 (1977).

[40] G. A. Lalazissis, S. Karatzikos, R. Fossion, D. Pena Arteaga, A. V. Afanasjev, and P. Ring, Phys. Lett. B671, 36 (2009).

[41] G. A. Lalazissis, T. Niksic, D. Vretenar, and P. Ring, Phys. Rev. C71, 024312 (2005).

[42] T. Niksic, D. Vretenar, and P. Ring, Phys. Rev. C. 78, 034318 (2008).

[43] A. Nikolaus, T. Hoch, and D. Madland, Phys. Rev. C. 46, 1757 (1992).

[44] Y. K. Gambhir and A. Bhagwat , Physics of Particles and Nuclei. 37, 194239 (2006).

[45] L5.N. Cooper, R.L. Mills, and A.M. Sessler, Phys. Rev. 114, 1377-1382 (1959).

[46] P. Ring and P. Schuck, The Nuclear Many-Body Problem (Springer- Verlag, 2004).

[47] S.G. Nilsson, I.Ragnarsson *Shapes and shells in nuclear structure* NewYork, USA :Cambridge University Press (1955).

[48] P.M. Walker, F.R. Xu and D.M. Cullen, Phys. Rev. C. 71, (2005) 067303.

[49] I. Maqbool, P. A. Ganai and J. A. Sheikh, Proceedings of the International Symposium on Nuclear Physics 54, 164 (2009).

[50] K. K. Girija, "Studies of shape changes of deformed nuclei and its effects on cluster emission" Masters thesis., University of Calicut, (2012).

[51] W. Nazarewicz and I. Ragnarsson in Handbook of Nuclear Properties, ed. Dorin N.Poenaru, Walter Greiner, (Oxford University Press, New York 2008) p. 80.

[52] N. Tajima, N. Suzuki, Phys. Rev. C. 64, 037301 (2001).

[53] R. K. Nesbet, Phys. Rev. 109, 1017 (1958).

[54] P. Ring, Y. K. Gambhir, and G. A. Lalazissis, Comp. Phys. Comm. 105, 77 (1997).

[55] P. Ring and P. Schuck, The Nuclear Many-Body Problem (Springer-Verlag, Berlin, 1980).

[56] G. N. Smirenkin, Report INDC(CCP)-359, 1993 (unpublished); also available at www-nds.iaea.org/ripl/.

[57] P. Möller, J. R. Nix, and W. J. Swiatecki, Nucl. Phys. A. 469, (1987).

[58] P. Möller and J. R. Nix, Nucl. Phys. A. 536, 20 (1992).

[59] P. Jachimowicz, M. Kowal, and J. Skalski, Phys. Rev. C. 85, 034305 (2012).

[60] J. Randrup and P. Möller, Phys. Rev. C. 88, 064606 (2013).

[61] T. Ichikawa, P. Möller, and A. J. Sierk, Phys. Rev. C. 87, 054326 (2013).

[62] S. Nilsson and I. Ragnarsson, Shapes and shells in nuclear structure, (Cambridge University Press, Cambridge 1995).

[63] A. V. Afanasjev, H. Abusara, P. Ring EPJ Web of Conferences 62, 03003 (2013).

[64] W. Koepf and P. Ring, Nucl. Phys. A. 493, 61 (1989).

[65] Y. Aboussir, J. M. Pearson, A. Dutta, and F. Tondeur, At. Data Nucl. Data Tables 61, 127 (1995).

[66] W. D. Myers and W. J. Swiatecki, Phys. Rev. C. 60, 014606 (1999).

[67] P. Möller, J. R. Nix, Nucl. Phys. A. 361, 117 (1981).

[68] P. Möller, J. R. Nix, At. Data Nucl. Data Tables 26, 165 (1981).

[69] P. Möller, J. R. Nix, W. D. Myers and W. J. Swiatecki, At. Data Nucl. Data Tables 59, 185-381 (1955).